applied sciences

Article

PD-Based Iterative Learning Control for the Nonlinear Low-Speed-Jitter Vibration of a Wind Turbine in Yaw Motion

Tingrui Liu and Zhifeng Nie *

College of Mechanical & Electronic Engineering, Shandong University of Science & Technology, Qingdao 266590, China; liutingrui@sdust.edu.cn
* Correspondence: sdjnnzf@163.com

Abstract: Aiming at the nonlinear low-speed-jitter (LSJ) vibration suppression for a yaw system of a megawatt wind turbine, a kinematics mechanism of the yaw system is investigated from the perspective of tribology, and a kinematics model of the yaw system based on an equilibrium position is established. On the basis of the dynamic modeling of the yaw system, a nonlinear mathematical model of the LSJ system is deduced. Based on the two lead motors' driving of the conventional yaw motion, an innovative design with a special installation of two auxiliary motors for yaw transmission is carried out, which is integrated with a matching centralized lubrication system (CLS). Based on open-loop proportional-derivative (PD) control and the iterative learning control methods of the time-varying continuous system, the stability control and jitter amplitude suppression of the yaw system are realized by using a combined driving torque provided by the lead and auxiliary gears. From the stability and convergence of the time-domain response and the convergence of the iterative error, the effectiveness of the iterative learning control method with the PD-based regulation is verified, and its advantages for engineering applications are shown based on the algorithm solver improvement. The feasibility of the physical realization and engineering application of the control methodology is verified by using controller-hardware-in-the-loop (C-HITL) simulation technology.

Keywords: low-speed jitter; yaw system; dynamic modeling; PD control; iterative learning control; hardware-in-the-loop simulation

Citation: Liu, T.; Nie, Z. PD-Based Iterative Learning Control for the Nonlinear Low-Speed-Jitter Vibration of a Wind Turbine in Yaw Motion. *Appl. Sci.* **2024**, *14*, 1750. https://doi.org/10.3390/app14051750

Academic Editors: Miaolei Zhou and Rui Xu

Received: 25 December 2023
Revised: 16 February 2024
Accepted: 18 February 2024
Published: 21 February 2024

1. Introduction

In order to improve the efficiency of wind power generation, wind turbines are moving towards a large-scale development. While developing them on a large scale, it is also necessary to make them as efficient, safe, and reliable as possible, which makes the safety of wind turbine blades and towers very important. Therefore, it is necessary to investigate the fracture failure and vibration issues of large wind turbine blades and towers. The destructive fracture phenomena of megawatt wind turbine blades and towers that have occurred around the world in recent years also indicate the necessity of studying this issue [1,2]. In the past decade, the research on wind turbine blade vibration has generally focused on the problem of the stall-induced nonlinear aeroelastic stability of blades (i.e., stall flutter in coupled vibrations under the combined action of structural nonlinearity and aerodynamic nonlinearity [3], linear classical flutters at high wind speeds [4], and fracture failures caused by vibrations from various turbulence and wake effects) [5]. From the perspective of wind fields, some scientific research institutes have established systematic methods for the ultimate structural failure of wind turbines under extreme wind conditions through the three-dimensional (3D) computational fluid dynamics (CFD) simulation of complex wind field characteristics and the aeroelastic coupling analysis of turbine structures [6]. The wind turbine structure mentioned here not only includes large blade systems, but also includes engine room systems and tower structures.

The tube sections of large wind turbine towers are usually made of Q345 steel plates with different thicknesses and rolled into a conical tube structure. Then, several tube sections are welded into "long sections", and every two "sections" are connected by flanges and bolts. In recent years, tower structures made of special composite materials (below 5 megawatts) have emerged, which have superior strength and a comprehensive performance, but low production results and expensive prices [7]. Therefore, most manufacturers still conduct research on large wind turbines above 5 megawatts based on steel structure towers, and scholars have also conducted many studies on this basis. For instance, Sadowski [8] used a composite steel beam element with metal wheels as the basic element of the tower body and applied finite element software to study the deformation of the tower body. Zhu et al. [9] used a finite element analysis to analyze the coupling behavior of the tower body and blades, and achieved an optimal design of the structure. Ajaei et al. [10] conducted a finite element analysis on the bolt positions at the connecting flanges between tower sections, exploring the mechanisms of explicit faults and fracture failure issues.

In order to balance the aerodynamic forces on multi-blade wind turbines, while increasing the power, effectively reducing the aerodynamic imbalance forces on the rotor and tower and reducing the fracture failures caused by unbalanced impacts, megawatt wind turbines must use the yaw motion to perform windward deflection and positioning [11,12]. However, during the yaw motion process, the vibration itself, especially the long-term significant LSJ vibration, can also cause safety hazards. Actually, the yaw phenomenon widely occurs in the motion process of many rotating power equipment and fluid-driven power systems; so, the stability of the yaw motion and the stability of the auxiliary motion, as well as the additional effects created by yaw, have been a hot topic for a long time, with modeling theories of various vibration systems and vibration control methods being the focus of the research. The representative studies are as follows. Le et al. [13] proposed a solution to the yaw tracking control problem of unmanned helicopters, transforming non-affine nonlinear equations into simplified affine models, estimating unknown parameters using the Levenberg–Marquardt algorithm, and implementing autonomous flight using an adaptive controller based on Lyapunov. Roshanbin and Preumont [14] investigated a new control mechanism to generate the yaw control torque of a hovering robot hummingbird. This method generates the yaw moment of the wing by modifying the kinematics of the wing, while minimizing its impacts on the roll and pitch moments. Saunders and Nagamune [15] introduced a fatigue load controller design for a semi-submersible floating offshore wind turbine. The designed controller was used to manipulate the pitch angles of three blades and minimize the fatigue load at the tower base, with the turbine position controlled by the cabin yaw angle and average wind speed. Therefore, with the expansion of wind turbines, the yaw effect and yaw control of wind turbines, especially megawatt wind turbines, are also worth studying. Various advanced control methods and theories have been applied and implemented. For example, Elkodama et al. [16] summarized and discussed the yaw control system, considering various control strategies for multi-objective control technology in different operating areas. For each control system, the different control algorithms are usually divided into classical, modern computing, and artificial intelligence. Modern and soft computing technologies have shown significant improvements in the system's performance with minimal costs and faster responses. For example, soft computing control algorithms, such as fuzzy logic control, sliding mode control, and maximum power point tracking, have shown superior performances. Dai et al. [17] established a dynamic coupling model for a multi-source driven yaw system. Different yaw angle control modes were studied, including comparative control and servo control. This model establishes a multi-channel electronic supply system, gearbox system, and hydraulic braking subsystem, achieving the coupling of the multi-channel yaw subsystem.

Since the wind direction is random and time-varying, it is difficult to accurately and immediately predict the wind direction and the target yaw angle. Yaw control based on the predicted wind direction is limited by the accuracy of the wind direction prediction, which leads to a small improvement of the energy capture efficiency of wind turbines. To address this issue, a stochastic model based on the intelligent scene generation (SG) was proposed to predict yaw actions to improve the energy capture efficiency [18]. In addition, over the years, comprehensive research has been conducted on the physical characteristics and effectiveness of the active yaw control of wind turbines under different wind conditions based on wind tunnel experiments and various analytical wind farm models [19]. These studies extensively discussed the distribution and relationship of the optimal yaw angle, wind farm size, and peak power gain, elucidating the effects of turbulence intensity and flow spacing on active yaw control.

The stability and time response analyses of the yaw motion and stability of the controller itself are also important topics in yaw system research, which requires that the proposed control method supplies the controlled object with better stability and motion trajectory, and also has the convenience of software development and the physical feasibility of hardware implementation, so as to further improve the maneuverability of active control and provide a theoretical basis for the design of wind turbine structures and yaw control strategies considering dynamic yaw operations [14,20,21]. For example, Liu et al. proposed a robust fractional proportional integral derivative (PID) controller design for yaw control systems [22], including a three-dimensional stable region analysis method for achieving fractional order control. Unlike other traditional stable region analysis methods, the proposed method [22] optimized other parameters based on robust design criteria for parameter uncertainty. Therefore, the controlled system can tolerate different parameter uncertainties, meet the transient performance index demands, and maintain the stability of the system. Based on the nonlinear fuzzy observation, active rear-steering and direct-yaw moment coordinated control were carried out, and the stability of the fuzzy sliding mode controller was proved by using the Lyapunov method to improve the yaw and roll stability control under extreme conditions [23]. Meanwhile, the combination of HITL simulation technology with LabVIEW/Casim demonstrates that the proposed fuzzy controller greatly improves yaw stability under extreme conditions. The LabVIEW 2020/Casim 2019 software suite can predict the braking performance, smoothness, power performance, and economy of the yaw turning motion.

For the megawatt wind turbine yaw system, a typical low-speed servo motion system is composed of a yaw sliding bearing and yaw drive system. Therefore, a friction self-excited vibration in low-speed motion, that is, a yaw crawling motion, inevitably occurs in the megawatt wind turbine yaw system during its operation, which affects the stability of the yaw motion and the accuracy of the yaw system [24]. Therefore, engineers and technicians have investigated the kinematics mechanism of the yaw system from the perspective of tribology, established the crawling kinematics model on the basis of equilibrium position, and analyzed the motion law and influencing factors of the yaw system, which had positive practical significance for the engineering application of megawatt units. As for the controlled system with a repetitive crawling motion, especially for the nonlinear crawling vibration system, iterative learning control [25] has unique tracking and estimation advantages for nonlinear repetitive crawling vibration. Especially, by using PID controllers, reinforcement learning techniques can promote the convergence of system responses and accelerate the running speed of the iteration process [26]. On the one hand, it can have a good tracking effect on the target value; on the other hand, it can be combined with a PID controller to limit the controlled object within the allowable error range and force the controlled object to exhibit a convergence trend [27].

The LSJ vibration is a rapid shaking phenomenon based on the aforementioned crawling phenomenon, which is a special case of crawling phenomenon. In extreme wind conditions, it is more likely to cause destructive effects. In the present study, the iterative learning control for the nonlinear LSJ vibration amplitude of a wind turbine in yaw motion is investigated. Aiming at amplitude suppression for the LSJ vibration of the yaw system of megawatt wind turbines, the kinematics mechanism of the yaw system is studied from the perspective of tribology, and the kinematics model of the yaw system based on the equilibrium position is established. On the basis of this model, the nonlinear mathematical model of the LSJ system is constructed. Inspired by the dual-driven parallel control mechanism of pitch and yaw servos [2], based on the conventional lead gear of yaw driving, the auxiliary gear of yaw driving is designed and mounted. Based on the open-loop PD control and the iterative learning control methods of the time-varying continuous system, the stability control and jitter suppression of the yaw system are realized by using the combined driving torques provided by the lead and auxiliary gears. From the stability and convergence of the time-domain response and the convergence of the iterative error, the effectiveness of the iterative learning control method is verified. The feasibility of the physical realization and engineering application of the control algorithm is verified using C-HITL simulation technology.

The content of this study is engineering application-oriented. The main contributions of this work can be summarized in the following aspects: (a) in practice, based on engineering applications, a new type of additional motor drive design is adopted in the LSJ damping system, accompanied by a centralized lubrication system, effectively improving the stability of the system. (b) In theory, an iterative algorithm based on a PD controller is used to control nonlinear LSJ systems. By utilizing large-step simulation algorithms and hardware sampling, the running time of iterative algorithms is shortened, making them more suitable for engineering applications. (c) In terms of combining theory and practice, by utilizing the C-HITL platform, i.e., the software and hardware combination method by way of OLE (object linking and embedding) for process control (OPC) communication, any complex intelligent algorithm can be indirectly applied to conventional controller hardware, which actually proposes an engineering application approach for complex intelligent algorithms. (d) The LSJ vibration control is a rarely studied topic, but its harmfulness is becoming increasingly apparent under extreme working conditions. At present, the LSJ control in some studies is based on a qualitative control method established on the basis of constant speed, slowly varying the yaw angle control. The LSJ control in the present study is an integrated control method based on a nonlinear LSJ displacement and nonlinear yaw angle, which has more engineering practical significance and is convenient for dealing with extreme working conditions.

The knowledge gap that this study intends to bridge is also related to the following aspects. The types of yaw systems are mainly divided into two categories [28]: one is the sliding bearing yaw system, as shown in this study, and the other is the rolling bearing system. At present, neither of these commercial systems has established or matched LSJ suppression system methods, and both are simplified through the intermittent application of lubricating oil [29]. Therefore, another advantage of this study is the design of an intelligent algorithm for performing matching [30,31], which not only drives the auxiliary motor, but also achieves dynamic lubrication, characterized by dynamic changes in the rolling friction coefficient. In the traditional jitter control method, a performance balance method between worm gear self-locking and yaw braking mechanisms was also used to achieve limited LSJ suppression [32], which is a local and passive suppression method. The characteristics of this passive suppression method include stiffness adjustment design, finite element analysis method, and linear LSJ amplitude suppression based on the assumption of a constant yaw rate [33–35]. However, the active dynamic control method adopted in the present study not only achieves amplitude suppression, but also frequency suppression, and it can directly handle nonlinear systems, which has a positive significance for engineering applications. Of course, in the end, this design also explores the theoretical method [36,37] of handling nonlinear systems based on a linear analysis with linear matrix inequality (LMI), as a purely theoretical discussion compared to engineering application methods.

2. Modeling of the Dynamic System

Figure 1 shows the main structure and components of the yaw system. The conventional medium-sized yaw system was configured and installed with only two yaw drive lead motors that were fixed to the initiative (active) driving unit. The two yaw drive auxiliary motors were specially configured and installed in the present study, which were embedded in the passively driven unit and located between two active motors, as displayed in Figure 1a,b. Figure 1b is the engineering schematic diagram with the auxiliary motor embedded in the driven second unit. The first unit includes the rack and its ancillary equipment as well as the engine compartment, while the driven second unit only includes the engine compartment and its sealing components [28].

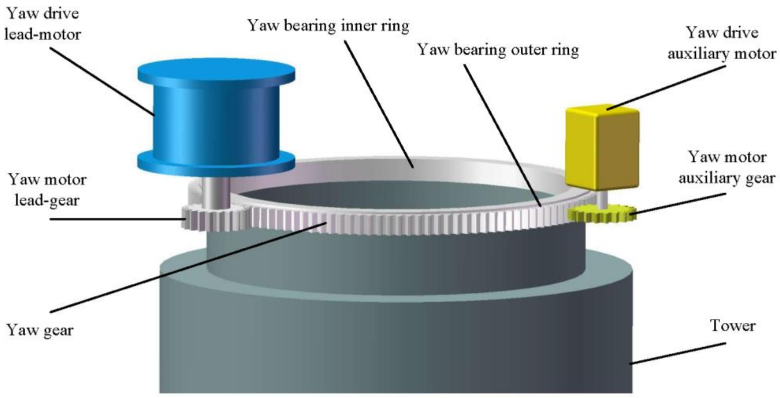

(a)

(b)

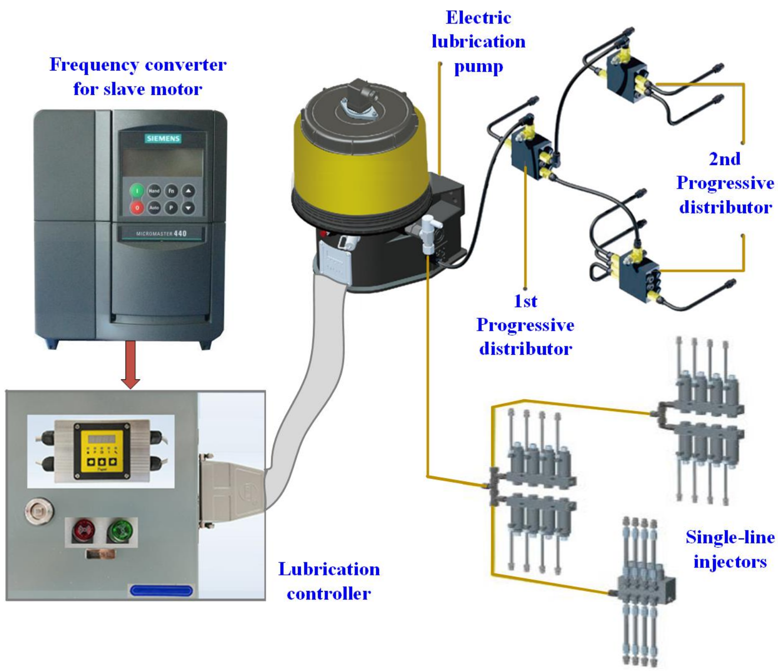

(c)

Figure 1. The main structure and components of the yaw system: (**a**) structural design for the dual-motor system; (**b**) engineering schematic diagram with the auxiliary motor embedded in the driven second unit; (**c**) CLS schematic diagram.

In the conventional yaw motion system, the yaw system controller sends a command signal, the two lead motors start synchronously, the yaw gear ring is fixed, and the yaw motors drive the yaw reduction gearbox to drive the main frame and engine room to slowly rotate around the yaw gear ring that is fixed to the tower flange with high-strength bolts. Due to the high mass of parts in the engine room, the yaw speed is extremely low. The yaw action of the megawatt wind turbine is characterized by the typical features of low speed, large load, and friction braking, which lead to LSJ vibrations due to the obvious, uneven speed during the operation, especially when the yaw is initiated and yaw brakes are applied. When the wind speed and direction change dramatically, the LSJ vibration is particularly severe. The LSJ vibration in the yaw system using sliding bearings comes from the crawling phenomenon between the yaw sliding pad (cushion) and the gear ring due to poor lubrication. Therefore, a centralized lubrication system (CLS) was designed in the present study, which was a controlled system that could perform dynamic lubrication.

The working process and highlight points of the auxiliary motors were as follows:

- A CLS schematic diagram was designed (Figure 1c), which was parallel to the auxiliary motor and driven by the same frequency converter. The output voltage of the frequency converter was 220V-690VAC. The CLS used a complete set of oil supply devices, which could supply oil to multiple lubrication points [29]. It was divided into progressive lubrication systems and single-line lubrication systems. A progressive system generally consists of four basic components: an electric lubrication pump, progressive distributors, pipeline components, and a control system. The single-line lubrication system can be regarded as a safety redundant structure of the progressive lubrication system. The amount of dynamic fuel supply was directly proportional to the voltage of the frequency converter, which also caused dynamic changes in the dynamic friction coefficient.
- There were lubricating oil holes on the surface of the sliding pad, which were injected by the lubrication system. Associate the driving voltage of electric lubrication pump with the driving voltage of the frequency converter of the auxiliary motor, and the two are direct proportion to each other. When the wind speed and direction changed dramatically, the proportion coefficient could take a larger value. When the driving voltage of the auxiliary motor was high, it meant an increase in the frictional resistance and an intensification of the LSJ vibration. At this time, an equal proportion of the driving voltage was applied to the electric pump, promoting a more lubricant injection to keep the sliding pad running smoothly and reduce the wear.
- During the yaw start phase, the electric lubrication pump was also activated, causing the amount of lubrication received by the sliding cushion to vary with the driving voltage of the auxiliary motor. This correlation change persisted until the end of the yaw process. The lubrication amount was dynamic, and the lubrication effect was controllable, which could minimize the LSJ vibration as much as possible. The driving voltage of the auxiliary motor should be much lower than that of the lead motor. There was no relationship between the voltage of the lead motor and the electric lubrication pump. In addition, the centralized lubrication system was uniformly controlled by a programmable logic controller (PLC) system. The PLC is an assembly controller system that controls all controlled processes in this design, including subsequent iterative algorithm control processes.

2.1. Analysis of the LSJ Vibration Mechanism

We used the simplified physical model developed by Zhao et al. [24] to explain the physical essence of the LSJ phenomenon in the yaw system, as shown in Figure 2a, and assumed that the part connecting the yaw lead motor and the load was the active driving first unit, and the shaking part of the load was the passively driven second unit. Note that the auxiliary motor associated with the CLS system is precisely embedded in the driven second unit (see Figure 1b). In Figure 2a, the active part (1) pushes the driven part (2) at rotational speed ω. k_1 is the stiffness coefficient; c_1 is the viscous torsional damping coefficient between friction surfaces and transmission parts. Due to the existence of rotational speed ω, with the push of the active part, 1, the spring repeats the processes of energy storage and energy release, and the driven part, 2, repeats the processes of acceleration and deceleration, thus forming a circular “sticky-sliding” jumping motion, forming a low-speed shaking microvibration, which is the mechanism of the LSJ. Figure 2b is the vibration model of the yaw system.

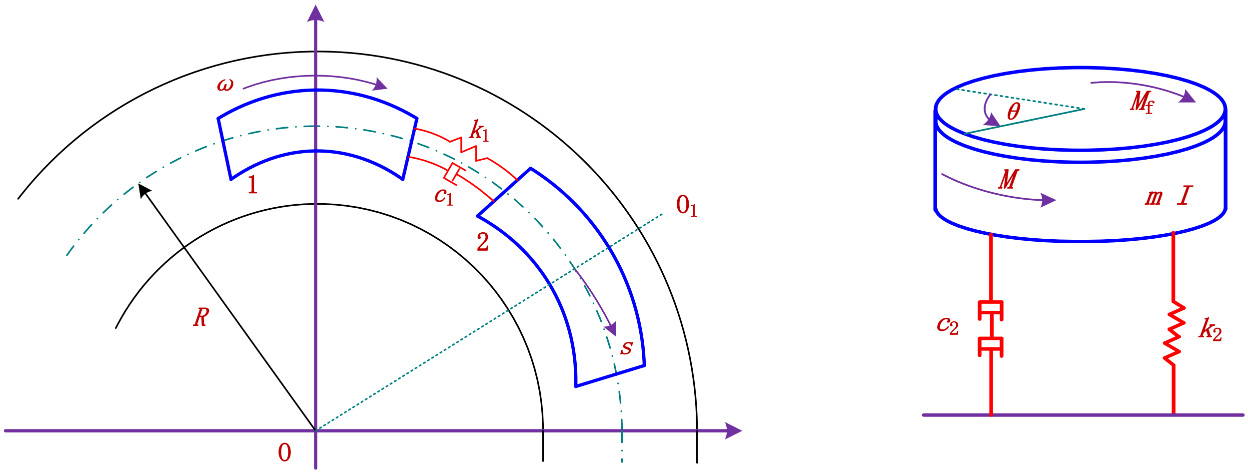

(**a**) (**b**)

Figure 2. Models: (**a**) LSJ physical model; (**b**) vibration model of the yaw system.

Firstly, assuming that the active component (1) slowly moves clockwise for a certain distance, s_0, the driving moment generated by the spring due to compression is exactly equal to the maximum static friction moment, M_j, experienced by the driven component, 2, i.e., $k_1 s_0 = M_j$; then, object 2 begins to move. Assuming that the distance of object 2 moving after time t is s, the differential equation for the motion of object 2 is:

$$J\frac{d^2S}{dt^2} + c_1\frac{dS}{dt} = -M_d + k_1(s_0 + R\omega t - s), \quad (1)$$

where J is the moment of inertia; c_1 is the torsional damping; $k_1(s_0 + R\omega t - s)$ is the driving moment; and M_d is the dynamic friction moment.

In order to simplify the analysis, the dynamic friction moment, M_d, is regarded as being composed of two parts: the constant component, M, and component $h\frac{ds}{dt}$ that varies with the rotary speed, namely $M_d = M + h\frac{ds}{dt}$. The static friction moment, $\Delta M = M_j - M = T\Delta\mu$, is substituted into Formula (1) to obtain:

$$J\frac{d^2S}{dt^2} + (c_1 + h)\frac{dS}{dt} + k_1 s = T\Delta\mu + k_1 R\omega t, \quad (2)$$

where h is the damping attenuation coefficient characterized by $c_1 + h = 2\xi_1\omega_{n1} J$, herein $\omega_{n1} = \sqrt{k_1/J}$; $T\Delta\mu$ is the difference between the static friction torque and dynamic friction torque; T is the positive pressure torque; and $\Delta\mu$ is the difference between the dynamic friction coefficient and static friction coefficient (DFC/SFC). The values of the DFC/SFC vary within the range of 0.02~0.06, changing with the variation in the lubrication effect. The values of the structural parameters (SPs) can be found in Table 1.

Table 1. The values of structural parameters (SPs).

SP Items	Values
Moment of inertia of object 2, J	330.2 kg m^2
Radius, R	1.1575 m
Positive pressure torque, T	200 N m
Damping ratio, ξ_1	0.05
Difference between DFC/SFC, $\Delta\mu$	within [0, 0.1]
Spring stiffness, k_1	10 N m/rad
Spring stiffness, k_2	3.3×10^8 N m/rad
Damping ratio, ξ_2	0.04
Moment of inertia, I	6603.9 kg m^2
Change rate of friction moment attenuation, α	0.6
Static friction coefficient, μ	0.07
Pre-tightening torque of the bolt, T_0	1000 N m
Nominal diameter of the bolt, d	0.033 m
Total mass of yaw system, m	4929 kg

2.2. Vibration Mechanism of the Yaw System

The yaw system, including the tower body of a large wind turbine, can be equivalent to a disk supported by the torsion spring, k_2, and torsional vibration damping, c_2, as shown in Figure 2b. The total mass of the yaw system disk is m, the moment of inertia is I, and the radius is R. The torque generated by the yaw main motor acting on the disc is $M = R \times F$. The friction torque between the active yaw system and the tower is M_f. θ is yaw angle, with equilibrium position $\frac{d\theta(0)}{dt} = 0$ representing the position when the yaw moment just overcomes the friction moment. The differential equation of motion based on the equilibrium position is:

$$I\frac{d^2\theta}{dt^2} + c_2\frac{d\theta}{dt} + k_2 \cdot \theta = M - M_f, \tag{3}$$

Assuming that the position where the yaw moment, M, just overcomes the static friction moment, M_{f0}, is the equilibrium point position, then $M = M_{f0}$, and the friction moment, M_f, at any time can be described as an offset equation: $M_f = M_{f0} - \Delta M_f \frac{d\theta}{dt}$. By substituting the offset equation into Formula (3), the following formula can be obtained:

$$I\frac{d^2\theta}{dt^2} + c_2\frac{d\theta}{dt} + k_2 \cdot \theta = \Delta M_f \frac{d\theta}{dt} \approx K_\Delta(0)\frac{d\theta}{dt}, \tag{4}$$

where ΔM_f is the yaw moment attenuation coefficient; $K_\Delta(0)$ is the slope of ΔM_f at the coordinate origin.

From Equation (4), the free vibration equation of viscous damping can be obtained:

$$\left(k_2/\omega_{n2}^2\right)\frac{d^2\theta}{dt^2} + 2\omega_{n2}(\xi_2 - \eta)\frac{d\theta}{dt} + \omega_{n2}^2\theta = 0, \tag{5}$$

where $\omega_{n2} = \sqrt{k_2/I}$; $\eta = K_\Delta(0)/\left[2(Ik_2)^{0.5}\right]$; $K_\Delta(0) = \alpha M_{fs}$; and $M_{fs} = \mu R(mg + 300T_0/d)$. Herein, η is the yaw rotational friction instability damping ratio; α is the change rate of the friction moment attenuation; M_{fs} is the static friction moment between the yaw system and the upper surface of the yaw gear ring; T_0 is the pre-tightening torque of the bolt; and d is the nominal diameter of the bolt. The values of the SPs can be found in Table 1.

To solve the differential equations given by Equations (2) and (5), a variable replacement method was developed. In Equation (2), since the rotational speed of active part 1 is expressed as $\omega = \frac{d\theta}{dt}$, and ωt is a nonlinear quantity, we might as well assume that $x = \theta t$; then, there exists:

$$\frac{dx}{dt} = \frac{d\theta}{dt}t + \theta = \omega t + \theta, \tag{6}$$

$$\frac{d^2x}{dt^2} = \frac{d^2\theta}{dt^2}t + 2\frac{d\theta}{dt} = 0 \quad (7)$$

Substitute ωt from Equation (6) into Equation (2); rewrite Equation (2) as:

$$J\frac{\mathrm{d}^2S}{\mathrm{d}t^2} + 2\xi_1\omega_{\mathrm{n}1}J\frac{ds}{dt} + k_1s - k_1R\frac{dx}{dt} + k_1R\theta - T\Delta\mu = 0, \quad (8)$$

Substitute $\frac{d^2\theta}{dt^2}$ from Equation (5) into Equation (7); then, rewrite Equation (7) as:

$$(k_2/\omega_{\mathrm{n}2}^2)\frac{\mathrm{d}^2x}{\mathrm{d}t^2} + 2(\xi_2 - \eta)\omega_{\mathrm{n}2}\frac{dx}{dt} - 2(\xi_2 - \eta)\omega_{\mathrm{n}2}\theta - 2I\frac{d\theta}{dt} + \omega_{\mathrm{n}2}^2x = 0, \quad (9)$$

Considering that, in conjunction with Formulas (8), (5), and (9) in turn, the state variables vector is $X = [x_1\ x_2\ x_3]^{\mathrm{T}} = [s\ \theta\ x]^{\mathrm{T}}$, we can obtain the following governing system:

$$M_0\ddot{X} + C_0\dot{X} + K_0X = B_0, \quad (10)$$

where M_0, C_0, and K_0 are 3×3 matrices; B_0 is 3×1 matrix and can be expressed as $B_0 = [T\Delta\mu\ 0\ 0]^{\mathrm{T}}$.

In the present study, in Equation (5), we assume that the force yaw moment applied to the right side of Formula (5) is u, based on the position of the equilibrium point. In Figure 1, the yaw driving auxiliary motor was also used for the active drive to overcome the LSJ vibration, with the driving action taking place exactly at the position of object 2 perpendicular to the direction of $O - O_1$ in Figure 2a. Assuming that the auxiliary driving torque of the yaw auxiliary motor is $0.2u$ (not exceeding $0.5u$, otherwise it will greatly affect the yaw torque), then the governing system in Equation (10) can be rewritten as:

$$M_0\ddot{X} + C_0\dot{X} + K_0X = [0.2 \quad 1 \quad 0]^{\mathrm{T}}\ u = Q_0u, \quad (11)$$

Note that, due to $B_0 = [T\Delta\mu\ 0\ 0]^{\mathrm{T}}$, the practical auxiliary driving torque is $0.2u - T\Delta\mu$.

To carry on with the subsequent solutions, assume $Y = \left[X\ \dot{X}\right]^{\mathrm{T}}$; Equation (11) can be transformed into the state space as follows:

$$\begin{cases} \dot{Y} = AY + Bu \\ y = CY \end{cases}, \quad (12)$$

where $A = \begin{bmatrix} 0_{3\times3} & I_{\mathrm{E}(3\times3)} \\ -M_0^{-1}K_0 & -M_0^{-1}C_0 \end{bmatrix}$, $B = \begin{bmatrix} 0_{3\times1} \\ M_0^{-1}Q_0 \end{bmatrix}$, $C = I_{\mathrm{E}(6\times6)}$; herein, I_{E} is the identity matrix.

3. Iterative Learning Control Based on the Open-Loop PD Regulation

The open-loop PD control can be expressed as follows:

$$u_{k+1}(t) = u_k(t) + \left(\Gamma\frac{\mathrm{d}}{\mathrm{d}t} + L\right)e_k(t), \quad (13)$$

where L and Γ are learning gain matrices, i.e., $L = \mathrm{K_P} \times I_{E(6\times6)}$, $\Gamma = \mathrm{K_d} \times I_{E(6\times6)}$,respectively; herein, $\mathrm{K_P}$ and $\mathrm{K_d}$ are the proportional and derivative parameters of the PD controller, respectively. e_k is the error in the k-th iteration process.

The iterative learning control of the time-varying continuous system is based on the following theorem [25]. If the system described by Equations (12) and (13) meets the following conditions:

(a) $\|I_\mathrm{E}-C(t)B(t)\Gamma(t)\| \leq \overline{\rho} < 1$; (b) $Y_k(0) = Y_0(k=1,2,3,\cdots), y_0(0) = y_\mathrm{d}(0)$, then, when $k \to \infty$, there exist $y_k(t) \to y_\mathrm{d}(t), \forall t \in [0,\mathrm{T}]$ the controller design and convergence analysis are as follows:

From Equations (12) and (13), it can be seen that the system output is:

$$y_{k+1}(0) = \mathrm{C}Y_{k+1}(0) = \mathrm{C}Y_k(0) = y_k(0), \tag{14}$$

then, $e_k(0) = 0(k=0,1,2,\cdots)$, that is, the initial conditions are met.

The solution for differential equation $\dot{Y} = AY + Bu$ is:

$$\begin{aligned} Y(t) &= C\exp\left(\int_0^t A\mathrm{d}\tau\right) + \exp\left(\int_0^t A\mathrm{d}\tau\right)\int_0^t B(\tau)u(\tau)\exp\left(\int_0^\tau -Ad\delta\right)\mathrm{d}\tau \\ &= \mathrm{C}\exp(At) + \exp(At)\int_0^t B(\tau\Big)u(\tau)\exp(-A\tau)d\tau \\ &= \mathrm{C}\exp(At) + \int_0^t \exp(A(t-\tau)B(\tau)u(\tau)\mathrm{d}\tau, \end{aligned} \tag{15}$$

let $\Phi(t,\tau) = \exp(A(t-\tau))$; then:

$$Y_k(t) - Y_{k+1}(t) = \int_0^t \Phi(t,\tau)B(\tau)(u_k(\tau) - u_{k+1}(\tau))\mathrm{d}\tau, \tag{16}$$

Since $e_k(t) = y_\mathrm{d}(t) - y_k(t), e_{k+1}(t) = y_\mathrm{d}(t) - y_{k+1}(t)$, then

$$\begin{gathered} e_{k+1}(t) - e_k(t) = y_k(t) - y_{k+1}(t) = C(t)(Y_k(t) - Y_{k+1}(t)) = \\ \int_0^t C(t)\Phi(t,\tau)B(\tau)(u_k(\tau) - u_{k+1}(\tau))\mathrm{d}\tau, \end{gathered} \tag{17}$$

the following formula exists:

$$e_{k+1}(t) = e_k(t) - \int_0^t C(t)\Phi(t,\tau)B(\tau)(u_{k+1}(\tau) - u_k(\tau))\mathrm{d}\tau, \tag{18}$$

Substitute Equation (13) into Equation (18); then, the error of the (i+1)-th output is:

$$e_{k+1}(t) = e_k(t) - \int_0^t C(t)\Phi(t,\tau)B(\tau)\left[\Gamma(\tau)\dot{e_k}(\tau) + \dot{L}(\tau)e_k(\tau)\right]\mathrm{d}\tau, \tag{19}$$

Let $G(t,\tau) = C(t)B(\tau)\Gamma(\tau)$; then, according to the partial integration method, there exists:

$$\begin{aligned} \int_0^t C(t)B(t)\Gamma(t)\dot{e_k}(\tau)\mathrm{d}\tau &= G(t,\tau)e_k(\tau)|_0^t - \int_0^t \frac{\partial}{\partial\tau}G(t,\tau)e_k(\tau)\mathrm{d}\tau \\ &= (t)B(t)\Gamma(\tau)e_k(\tau) - \int_0^t \frac{\partial}{\partial\tau}G(t,\tau)e_k(\tau)\mathrm{d}\tau, \end{aligned} \tag{20}$$

Substitute Equation (20) into Equation (19); then:

$$\begin{gathered} e_{k+1}(t) = [I_\mathrm{E} - C(t)B(t)\Gamma(t)]e_k(t) + \int_0^t \frac{\partial}{\partial\tau}G(t,\tau)e_k(\tau)\mathrm{d}\tau - \\ \int_0^t C(t)\Phi(t,\tau)B(\tau)L(\tau)e_k(\tau)\mathrm{d}\tau, \end{gathered} \tag{21}$$

Perform the norm operation at both ends of Formula (21), and the following equation can be obtained:

$$\begin{gathered} \|e_{k+1}(t)\| \leq \|I_\mathrm{E} - C(t)B(t)\Gamma(t)\|\|e_k(t)\| + \int_0^t \left\|\frac{\partial}{\partial\tau}G(t,\tau)\right\|\|e_k(\tau)\|\mathrm{d}\tau \\ + \int_0^t \|C(t)\Phi(t,\tau)B(\tau)L(\tau)\|\|e_k(\tau)\|\mathrm{d}\tau \leq \|I_\mathrm{E} - C(t)B(t)\Gamma(t)\|\|e_k(t)\| \\ + \int_0^t b_1\|e_k(\tau)\|\mathrm{d}\tau, \end{gathered} \tag{22}$$

where

$$b_1 = \max\left\{\sup_{t,\tau\in[0,\mathrm{T}]}\left\|\frac{\partial}{\partial\tau}G(t,\tau)\right\|, \sup_{t,\tau\in[0,\mathrm{T}]}\|C(t)\Phi(t,\tau)B(\tau)L(\tau)\|\right\}, \tag{23}$$

Multiply $\exp(-\lambda t), \lambda > 0$ at both ends of Formula (22); consider $\int_0^t \exp(\lambda t)d\tau = \frac{\exp(\lambda t)-1}{\lambda}$ and the following can be obtained:

$$\begin{array}{c} \exp(-\lambda t)\int_0^t b_1\|e_k(\tau)\|d\tau = \exp(-\lambda t)\int_0^t b_1\|e_k(\tau)\|\exp(-\lambda\tau)\exp(\lambda\tau)d\tau \\ \leq b_1\exp(-\lambda t)\|e_k(\tau)\|_\lambda\int_0^t \exp(\lambda\tau)d\tau = b_1\exp(-\lambda t)\|e_k(\tau)\|_\lambda\frac{\exp(\lambda t)-1}{\lambda} \\ = \frac{b_1}{\lambda}\|e_k(\tau)\|_\lambda\exp(-\lambda t)(\exp(\lambda t)-1) = b_1\frac{(1-\exp(-\lambda t))}{\lambda}\|e_k(\tau)\|_\lambda \\ \leq b_1\frac{(1-\exp(-\lambda T))}{\lambda}\|e_k(\tau)\|_\lambda, \end{array} \tag{24}$$

then:

$$\alpha\|e_{k+1}\|_\lambda \leq \tilde{\rho}\|e_k\|_\lambda, \tag{25}$$

where $\tilde{\rho} = \bar{\rho} + b_1\frac{1-\exp(-\lambda T)}{\lambda} + b_2\left(\frac{1-\exp(-\lambda T)}{\lambda}\right)^2$. Since $\bar{\rho} < 1$; then, when λ is large enough, $\tilde{\rho} < 1$ exists. Hence, $\lim_{k\to\infty}\|e_k\|_\lambda = 0$.

4. Numerical Analysis and Discussion

The related SP values follow the values given in Table 1. For the six state variables in Equation (12) that need to be controlled, we might as well assume that the initial value of the state variable vector is $q_i(0) = 0.01 \times [1\ 1\ 1\ 1\ 1\ 1]^T$, and the desired target trajectories are:

$$\begin{array}{c} q_{1d}(t) = q_{2d}(t) = q_{3d}(t) = 0.01\sin(3t); \\ q_{4d}(t) = q_{5d}(t) = q_{6d}(t) = 0.03\cos(3t), \end{array} \tag{26}$$

Figure 3 shows the simulation results of the uncontrolled LSJ displacement (s) and yaw angle (θ) under the condition of the external driving torque $u = 0$. It can be seen that, although the yaw displacement seems relatively stable, in reality, it is in a slow and gradual state of divergence. The LSJ displacement presents a large fluctuation peak within 30 s, with the maximum value reaching 0.05 m, that is, the peak value 0.05 m causes the physical fatigue and structural failure of the yaw system in the long-term fluctuation process. Therefore, the vibration control of the LSJ displacement is absolutely necessary, provided that the yaw displacement is controlled and converges.

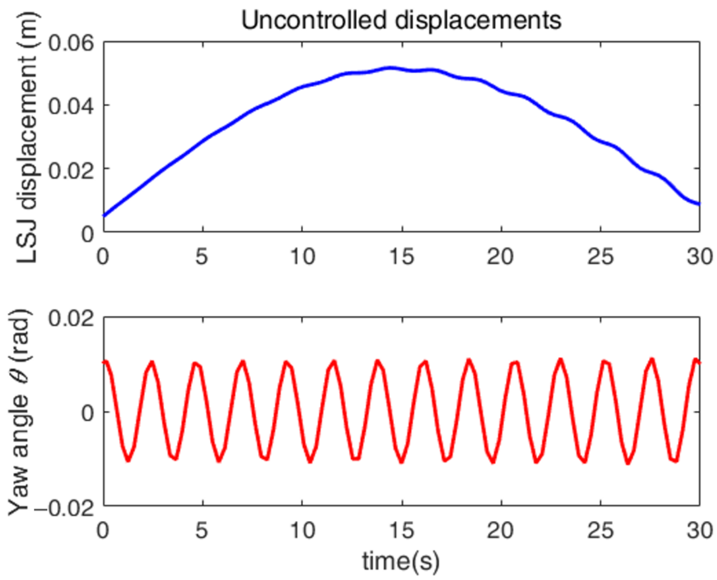

Figure 3. The uncontrolled displacements.

4.1. Amplitude Suppression from the Iterative Learning Algorithm

For the open-loop PD control in Equation (13), the learning gain matrices L and Γ are adjusted with $K_P = 20$, $K_d = 0.95$. To highlight the superiority of the iterative learning control algorithm, Figure 4 illustrates the three controlled displacements: LSJ displacement

$x_1 = s$, yaw angle $x_2 = \theta$, and intermediate variable $x_3 = x$, i.e., the simulation results in 40 iterations. It can be seen from the iterative processes of the LSJ displacements and yaw angles that the amplitudes of these two displacements become smaller and smaller as the number of iterations increases and illustrate trends of attenuation and convergence over time, which shows the effectiveness of the iterative algorithm. Due to $x_3 = x = \theta t$, along with the change in time, t, the compound variable, x_3, shows the trends of an equal-amplitude vibration or gradual attenuation, which shows the robustness of the iterative algorithm. In particular, the average amplitude of LSJ vibrations in 40 iterations is lower than 0.004 m, which is far less than the amplitude of the uncontrolled LSJ displacement (that is, 0.05 m in Figure 3), reflecting the effectiveness of jitter suppression.

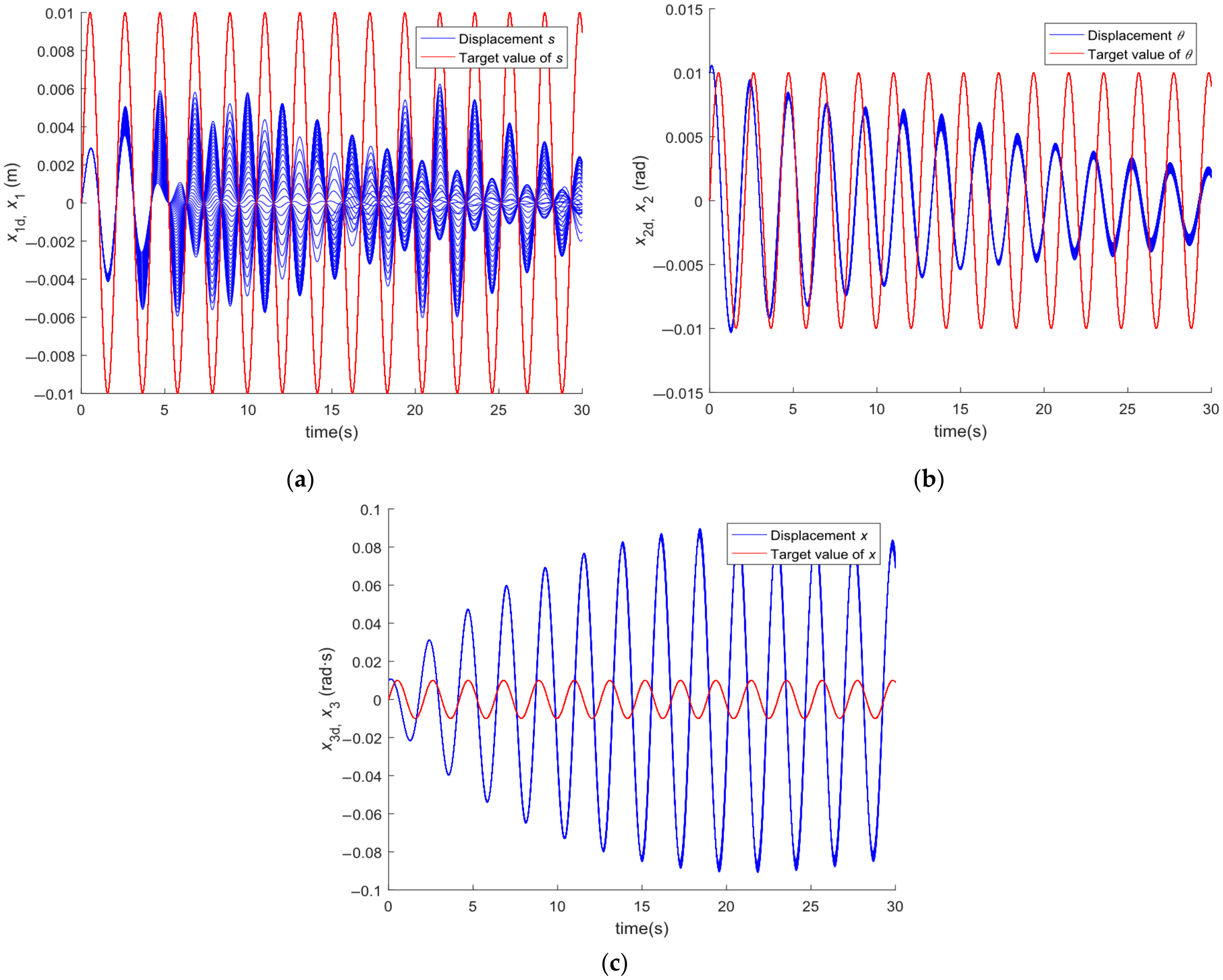

Figure 4. The three controlled displacements illustrated by the simulation results in 40 iterations: (**a**) LSJ displacement $x_1 = s$; (**b**) yaw angle $x_2 = \theta$; (**c**) another compound variable with no physical meaning, x_3.

Frequency control is also an interesting and positive topic. From the fluctuation frequency of the controlled signal, the frequency of the signal in the iteration process basically follows the predetermined frequency of the target signal, that is, when we change the frequency of the target signal, the frequency of the controlled signal changes accordingly, which actually achieves the goal of frequency control, and which is another advantage of the iterative algorithm.

In addition, as for the target values x_{1d} and x_{2d}, the role of these target values is to set an ideal range to make the controlled object fluctuate within this range under the control of u_1 and u_2, not exceed this range, and attenuate as much as possible with the increase in the number of iterations. As for the target value x_{3d}, the values of x_3 in the 40 iterations exceed the range of x_{3d}. This is because we did not actually control x_3, which was just a follow-up intermediate variable including time, t. However, as long as variable x_3 gradually attenuated over time, t, or could maintain a constant-amplitude vibration, it could exactly verify the effectiveness of the real-time control of x_1 and x_2.

4.2. Discussion of the Iterative Learning Algorithm

Figure 5 illustrates the results of the three displacements in the last iteration process, the driving torques of the lead gear (u_2) and auxiliary drive gear (u_1), and the changes in the maximum absolute values of error $i (i = 1, 2, 3)$ with the iterative times during the 40 iterations for the three controlled displacements. As mentioned above, the auxiliary driving torque, $u_1 = 0.2u_2 - T\Delta\mu$, fluctuates within a reasonable range and is physically realizable.

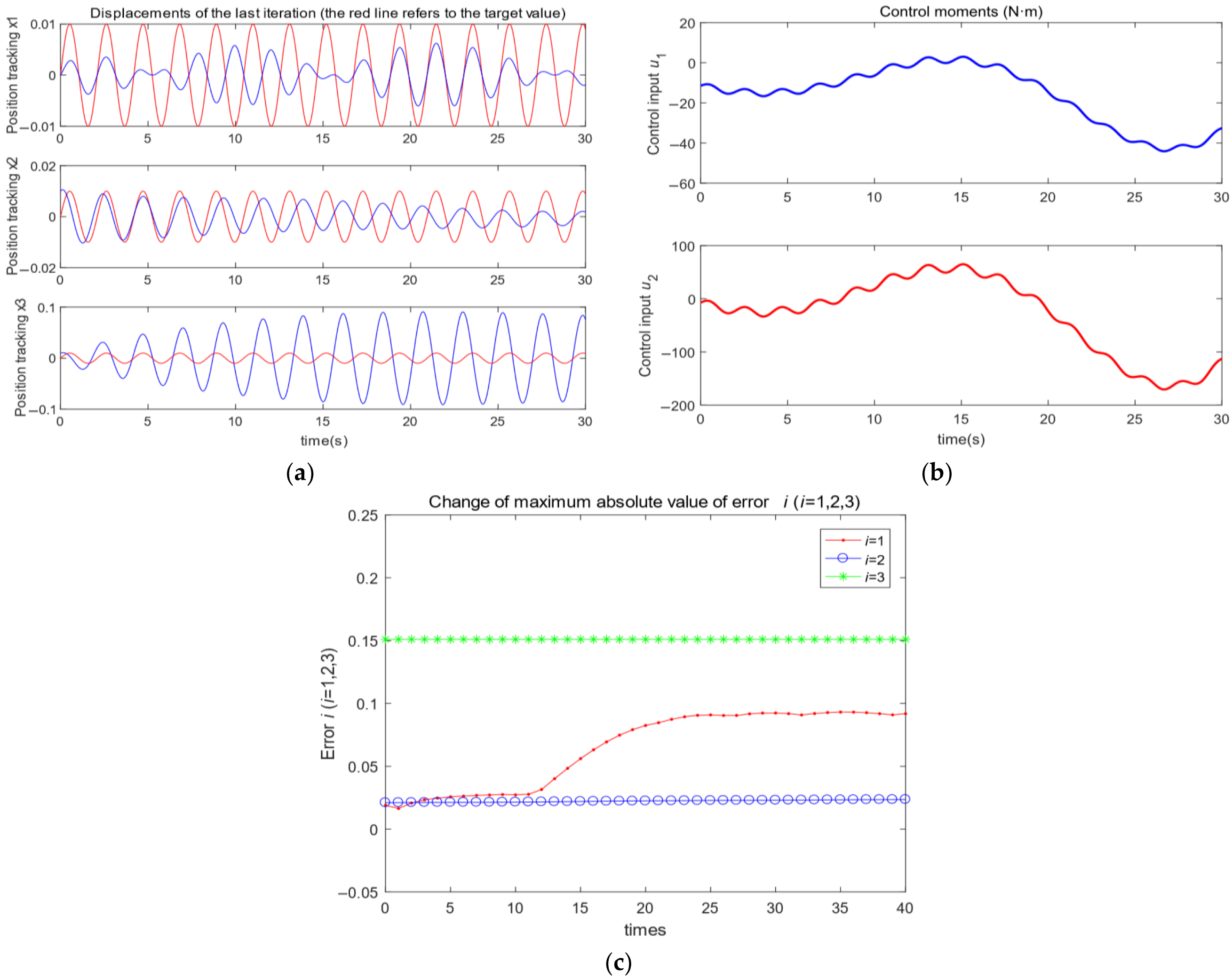

Figure 5. Illustrations: (**a**) results of the three displacements in the last iteration process; (**b**) control input signals (u_1 and u_2); (**c**) changes in maximum absolute values of errors with iterative times.

From the perspective of maximum errors, during 40 iterations, the errors of the yaw angles were basically kept near 0.02 rad, which reflected the effectiveness of yaw tracking and the stability of the yaw process. The tracking errors of the composite variable, x_3, were basically stable at 0.15 rad·s. This meant that, although the time component in the composite variable increased linearly, the composite variable remained stable as time progressed, which further proved the stability and convergence of the yaw motion, and further demonstrated the robustness of the iterative algorithm. The tracking errors of the LSJ vibration fluctuated between 0.082 m and 0.084 m after 25 iterations, indicating that the LSJ vibration was basically stable and no large jump occurred, thus achieving the goal of chatter control.

In the present study, the details of the iterative algorithm based on the PD controller needed to be elaborated further:

- The target value was set as a sine function with a certain frequency, so the results of the iterative algorithm were universal. In other words, if the target value was set as a constant value, the convergence control of the controlled displacement could be completely realized through the iterative control function;
- Formula (2) actually represents a nonlinear system, which is integrated into a formal linear system after variable replacement, as shown in Formula (11). The governing system in Equation (11) was actually an under-actuated system. The iterative algorithm based on PD control, whether dealing with nonlinear systems or under-actuated systems, presented unique advantages, which was exactly the reason why iterative the learning control algorithm was used instead of other control algorithms in this design. At the same time, the iterative algorithm combined with the PD parameter adjustment had significant advantages for both robustness and engineering practicability;
- In Figure 2a, the yaw drive auxiliary motor acted on the position of object 2, and the direction of the driving torque was perpendicular to the direction of $O - O_1$, so that the free vibration equation of Formula (2) would not be changed. As for the setting of control input signal u_1 as 0.2 times the value of the input signal, u_2, this occurred because an input signal that was too large, u_1, would have a reverse reaction, and an input signal that was too small, u_1, would have also weakened the control effect;
- Formula (13) was written as follows: $u_{k+1}(t) = u_k(t) + \left(\Gamma \frac{\mathrm{d}}{\mathrm{d}t} + L\right) e_{k+1}(t)$, that is, a closed-loop PD control with higher accuracy. We used an open-loop PD instead of a closed-loop PD here to speed up the controller hardware as much as possible on the premise of ensuring the control effect. This was also the reason why we adopted the PD control instead of a conventional PID control, which could greatly improve the running speed and considerably shorten the scanning cycle of the PLC system mentioned later on in the study.

4.3. Robustness and Practicability of the PD-Based Iterative Learning Algorithm

As mentioned above, the iterative algorithm combined with the PD parameter adjustment had significant advantages for both robustness and engineering practicability. In the present study, the dynamic adjustment of the PD parameters could be realized through the built-in PID tuning control (BPTC) panel in the STEP-7 MicroWin Software of S7-200 PLC. Because many cluster PD parameters can meet the aforementioned algorithm conditions, the BPTC panel can dynamically adjust and test the multi-cluster parameters. Of course, different PD parameters have different control effects, which is also a manifestation of the robustness of the algorithm. To test the robustness, another set of PD parameters with $K_{\mathrm{P}} = 1$, $K_{\mathrm{d}} = 3.5$, were used in the same controlled object as the processing case, and the results are shown in Figures 6 and 7.

The controlled displacements three are illustrated by the simulation results for 100 iterations by using the second set of PD parameters with $K_{\mathrm{P}} = 1$, $K_{\mathrm{d}} = 3.5$ in Figure 6. The results of the three displacements in the last iteration process, the control input signals (u_1 and u_2), and the changes in the maximum absolute values of errors with iterative times are illustrated in Figure 7 by using the second set of PD parameters with $K_{\mathrm{P}} = 1$, $K_{\mathrm{d}} = 3.5$.

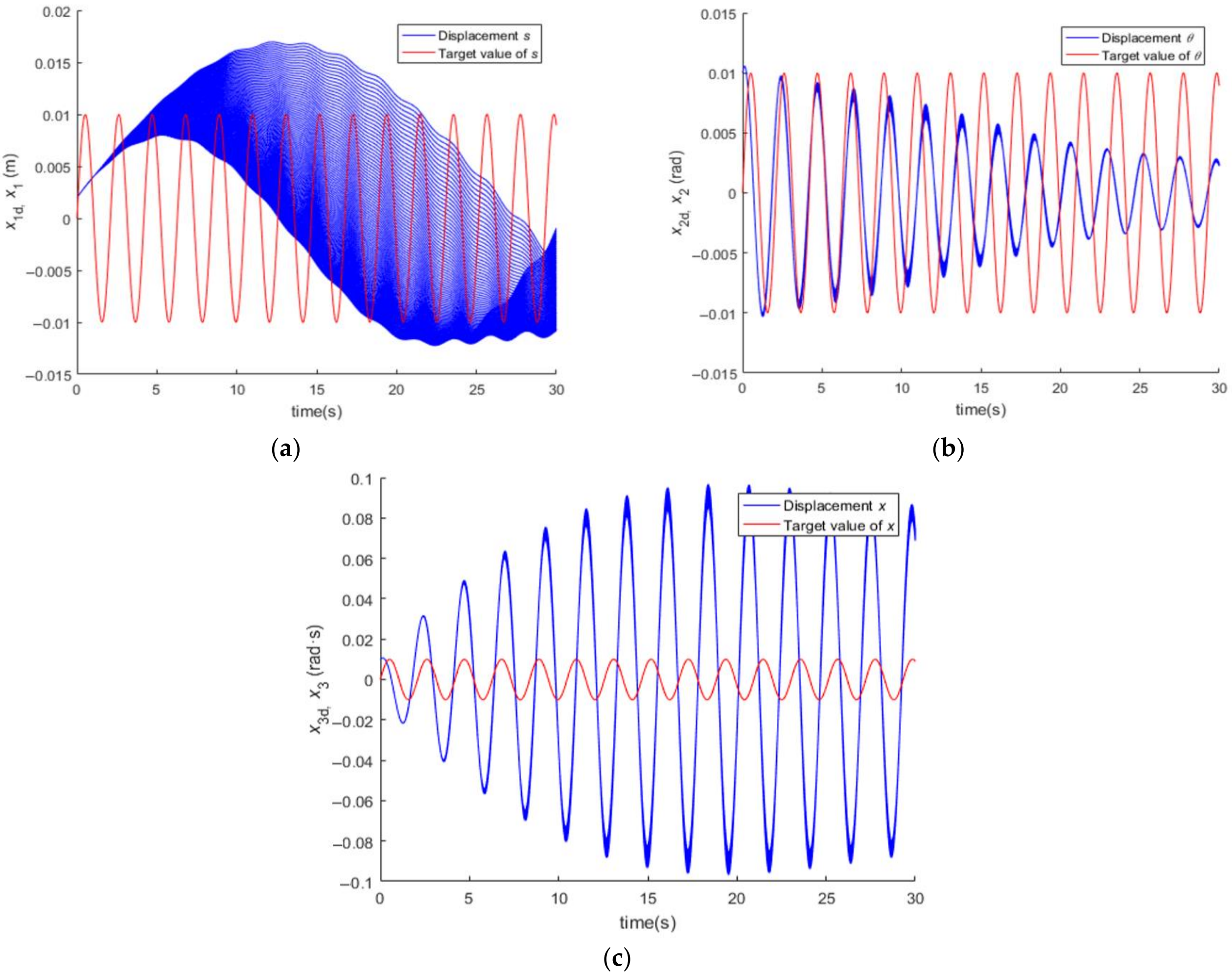

Figure 6. The three controlled displacements illustrated by the simulation results for 100 iterations by using the second set of PD parameters with $K_{\mathrm{P}} = 1$, $K_{\mathrm{d}} = 3.5$: (**a**) LSJ displacement $x_1 = s$; (**b**) yaw angle $x_2 = \theta$; (**c**) another compound variable with no physical meaning, x_3.

Compared with the results in Figures 4 and 5, in general, the results in Figures 6 and 7 maintain a similar control effect. For position variable x_1, although the latter is somewhat larger than the former in the controlled amplitudes, it still remains within the effective control range, and the fluctuation is more stable, which is another acceptable controlled effect.

As for the error margin of the PD-based iterative learning control for the LSJ vibration, it varied with the structural parameters of the system structure in Figure 1 and the parameters of the PD controller, but we could verify the rationality of error fluctuations using the limit range and standard deviation of errors during the iteration process. Table 2 shows the minimum, maximum, and standard deviation of the three types of errors in the two cases. The standard deviation of the first type of error in the first case is 0.02013 m, which is within the standard deviation range [0, 5%] of motion control errors for conventional yaw systems, reflecting a good LSJ control performance. The standard deviation values of the other five errors values are all very small, further verifying the effectiveness of the two sets of PD parameters and the robustness of the proposed control algorithms.

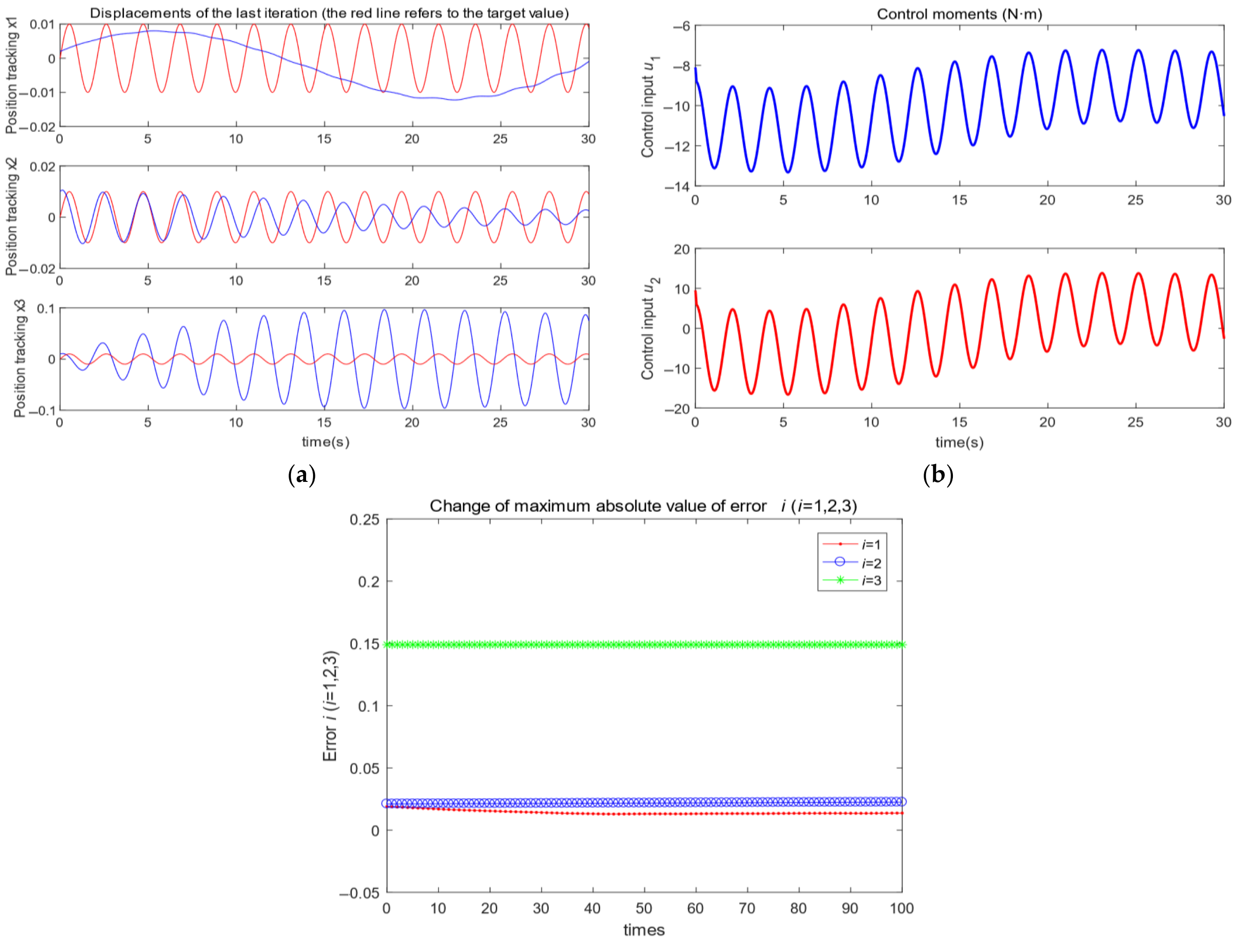

Figure 7. Illustrations created by using the second set of PD parameters with $K_P = 1$, $K_d = 3.5$: (**a**) results of three displacements in the last iteration process; (**b**) control input signals (u_1 and u_2); (**c**) changes in the maximum absolute values of errors with iterative times.

Table 2. The minimum, maximum, and standard deviation of the three types of errors.

Cases	Errors	Minimum	Maximum	Standard Deviation
$K_P = 20$, $K_d = 0.95$	Error 1 (m)	0.01644	0.08312	0.02013
	Error 2 (rad)	0.02013	0.02355	0.00081
	Error 3 (rad·s)	0.01518	0.01521	1.405×10^{-16}
$K_P = 1$, $K_d = 3.5$	Error 1 (m)	0.01292	0.01894	0.001579
	Error 2 (rad)	0.02103	0.02244	0.000406
	Error 3 (rad·s)	0.01478	0.01491	4.18×10^{-16}

As for the engineering practicability, because the PID parameters have a certain physical meaning of engineering regulation, the realization of the PID control process can be realized through many ready-made commercial controller hardware items, such as the built-in PID controllers of the aforementioned PLCs.

5. Practical Implementations in Engineering Applications

At present, the hardware controller of wind power systems mainly adopts a PLC system, which is also due to the reliability and wide adaptability of PLCs in analog process control, sequence control, and various motor system control applications. For example, the aforementioned lead motor and auxiliary motor can be easily controlled by the PLC controller system. In particular, in the simulation results in Figure 5, we can see that the two control input signals from the motors are more suitable for control implementations provided by the stepping motors. The PLC has built-in driving modules for various stepping motors, which can reliably and effectively drive the stepping motors.

5.1. Practical Implementation of the PD-Based Iterative Learning Algorithm by Using C-HITL Simulation Technology

In the present study, a virtual simulation platform was proposed to verify the feasibility of the controller hardware implementation for control algorithms. This was a platform using C-HITL simulation technology based on OPC communication [30]. To avoid the failure of the algorithm in the hardware implementation process due to the problem of hardware memory limitation and the cumulative error of calculations in the PLC hardware just mentioned, the C-HITL simulation was used to verify the feasibility of the hardware implementation of the control algorithm. For the software-in-the-loop simulation method and the HITL simulation technology [26,30] mentioned above, using the C-HITL platform, we not only demonstrated the feasibility of the software implementation of complex control algorithms, but also demonstrated the feasibility of the implementation of complex control algorithms in controller hardware, providing a feasibility analysis and reference for engineering applications.

In the C-HITL platform, the PLC CPU module runs the entire PD algorithm by using a built-in PD controller, sends the output signals to the PC to drive the governing system, Equation (12), and receives signals from the PC. The system model and iterative algorithm are run in the MATLAB/SIMULINK (R2022b, MathWorks, Natick, MA, USA) environment in the PC. Sending and receiving are performed through the OPC mechanism. OPC Read/Write blocks in SIMULINK can read or write signals from or into the PLC system by the OPC server.

The signals of the controlled displacements (s and θ) and the practical control inputs (u_1 and u_2) can be displayed by a human machine interface (HMI) connected to the PLC CPU. Figure 8a shows the C-HITL experiment plan based on OPC communication. Figure 8b demonstrates the practical control inputs (u_1 and u_2 in HMI) denoted by u_1 (blue mark) and u_2 (red mark) under the same simulation conditions mentioned in Sections 4.1 and 4.2.

The HMI in Figure 8b shows the process of dynamic fluctuations in the control input signals. The control inputs, i.e., control moments in Figures 5 and 8b, demonstrate almost the same changing trends and amplitudes of the control moments, and show a picture frame within time range [0 30s]. The numerical simulation and C-HITL experiment implementation show perfect consistency. As for the smoothness of the fluctuating curve in Figure 8b, it looks somewhat different from Figure 5 because the sampling time of the PLC hardware system (including the HMI display) is different from that of the simulation method in MATLAB. It should be noted that the HMI not only displays the control input signals, but also displays the real-time fluctuation processes of the controlled signals, which also shows the effectiveness of the C-HITL platform based on OPC technology, and further demonstrates the feasibility of the iterative algorithm to achieve engineering applications in the controller hardware.

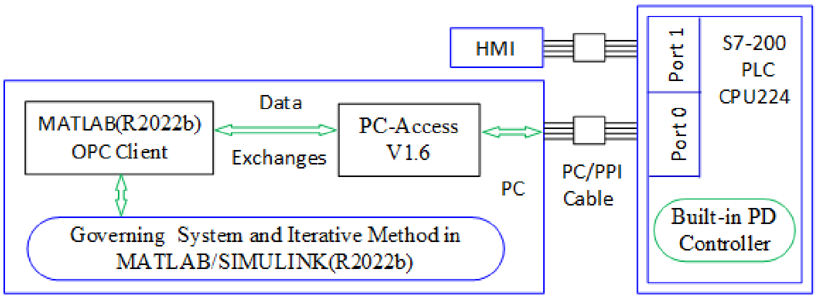

(**a**)

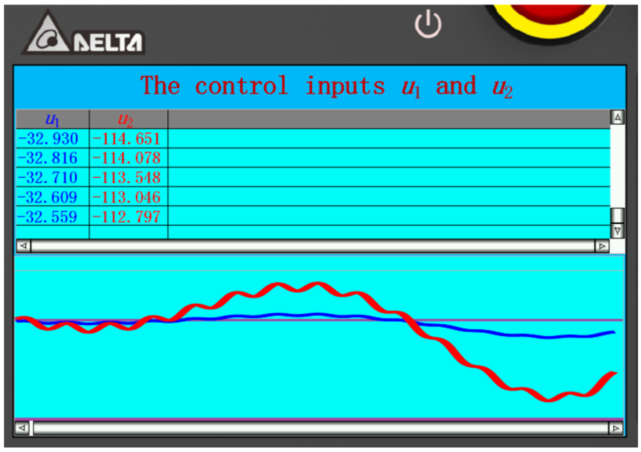

(**b**)

Figure 8. The C-HITL experiment plan illustrations: (**a**) C-HITL experiment plan based on OPC communication; (**b**) practical control inputs (u_1 and u_2).

5.2. Improvement of the Methodology Application

The most obvious limitation of the methodology application lies in the complex iterative process and great computational workload of the iterative algorithm, which is also very time-consuming. In order to accelerate the iterative algorithm and make the C-HITL platform apply to a more real-time scenario, numerical solutions with compromised step sizes that are suitable for both rigid and non-rigid systems, with lower accuracy rates, can be considered for the purpose of engineering applications.

During the simulation, we specified the integration order of MATLAB Solver. The Solver was set to an integration order of odeN [31] with a default setting of N_{ode} = 3, that is, the ode3 Solver with a third-order accuracy. In other words, this solver was used to integrate states into each time step of a simulation that used the nonadaptive odeN variable-step solver, which achieved a compromise between the fast fixed-step-size solution and adaptive variable-step-size solution. Compared with the conventional four-order Runge–Kutta method, its accuracy was lower. However, it could greatly improve the operation speed in the iterative process. The iteration time was only 1/20 for the former, which was more suitable for engineering applications.

Still, using the first case in Figure 4 as an example, Figure 9a shows the controlled two displacements, LSJ displacement $x_1 = s$ and yaw angle $x_2 = \theta$, by using the ode3 Solver. The two controlled displacements in Figures 4 and 9a show almost the same fluctuation amplitudes, except that the sampling step sizes are finite. However, the calculation speed greatly improved by only about 1/20 for the former. Figure 9b shows the changes in the maximum absolute values of error $i(i = 1, 2, 3)$ with iterative times during the 40 iterations for the three controlled displacements. The tracking errors of the LSJ vibration fluctuated between 0.085 and 0.095 after 25 iterations, which was still a very small fluctuation range, indicating that the LSJ vibration was basically stable and no large jump occurred, thus, in the same way, achieving the goal of chatter control.

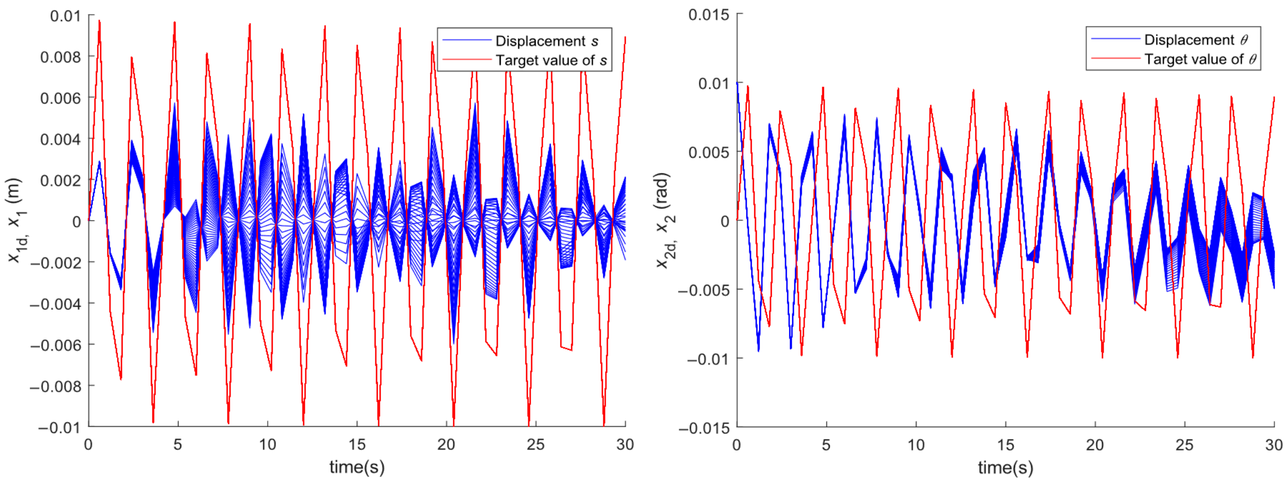

(**a**)

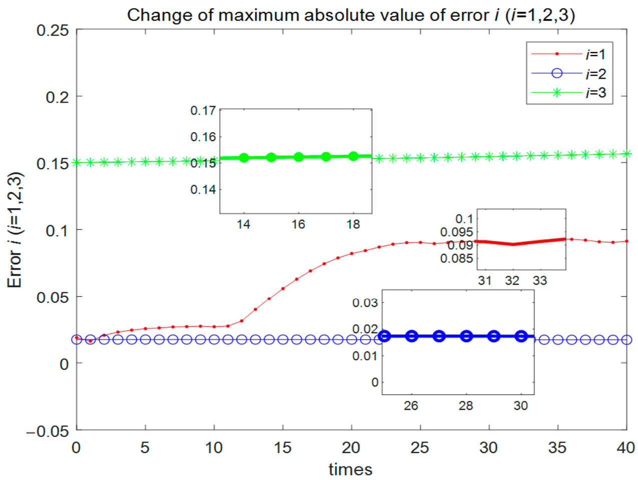

(**b**)

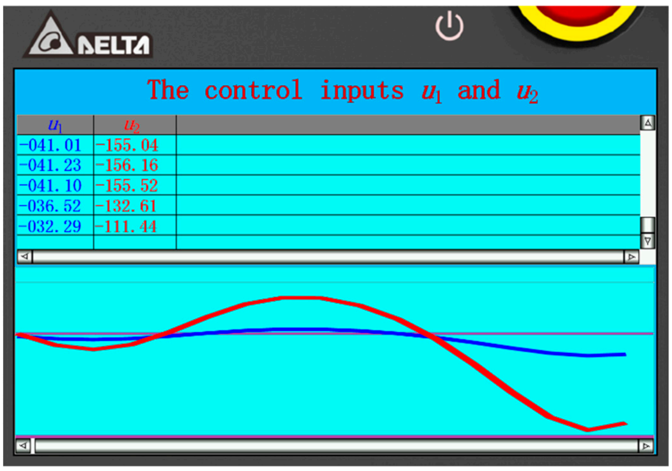

(**c**)

Figure 9. Illustrations created by using odeN Solver. (**a**) The controlled two displacements: LSJ displacement $x_1 = s$ and yaw angle $x_2 = \theta$; (**b**) changes in the maximum absolute values of errors with iterative times; (**c**) practical control inputs displayed by HMI by using odeN Solver.

Figure 9c shows the related, practical control inputs (u_1 and u_2) by way of the C-HITL platform by using the odeN Solver. Compared with the C-HITL platform in Figure 8b, the fluctuation curves in Figure 9c appear smoother, which was the result for the large-step and fixed-step simulations and sampling. However, the corresponding speed of the C-HITL platform was faster, approximately 1/40–1/30 of the former. In summary, we can use fixed-step software simulation and large-step hardware sampling to make the proposed methodology more widely applicable for the repeatability of the research elsewhere.

6. Practicality Comparison

Compared with the other existing results, the practicality of the results in the present study should be further explained. As mentioned in the related references [11–14,18,19] regarding power and yaw stability issues, as long as the chattering can be effectively controlled, under the control strategy proposed in this design, the yaw process can be fully stabilized and the power acquisition of the system will not be affected at all. The problems of the wind force magnitude and direction proposed in the references [15–17] can be uniformly summarized as disturbance problems in this design. However, PD-based iterative learning control has significant advantages when dealing with disturbances [25], so the control algorithm used in this design was actually an adaptive control algorithm with a robust performance, which could appropriately deal with wind disturbance. At the same time, the auxiliary motor driving method proposed in this design increased the driving torque from 10% to 30% or even higher (in the present study, it was only set at 20% and directly affected the LSJ system), which meant a better control performance and disturbance resistance. It can not only be applied to the control process of a single wind turbine, for resisting various types of flutter [1–4], but can also be used in the control processes of wake and eddy-current [5,6] disturbances in wind farm clusters.

In the current wind energy production process, most of the existing research results focus on the resonance problem of the wind turbine system caused by the blades, because an increase in the swept area of the impeller inevitably prolongs the length of the blades, which increases the mass and decreases the stiffness of the blades, reduces their inherent frequency, and enters the frequency band of impeller speed stimulation, leading to the resonance of the impeller unit. In fact, there are similar problems with tower structures. As a supporting structure system, the tower system constantly receives energy from the impeller system and also bears the load transmitted by the impeller system. If its natural frequency also enters the excitation frequency band of the impeller speed, coupling resonance occurs with the impeller system during the operation of the unit. This coupling of low-speed and low-frequency vibrations has a catastrophic impact on the operation of the unit. The design in the present study focused on the low-speed buffeting during the yaw process, and treated the load excitation in the related references [1–6,11–19] as a dynamic disturbance, thus achieving stability control. Based on the proposed iterative algorithm using the open-loop PD, further research on the coupling resonance of the impeller tower has a positive significance for reducing the incidence of wind turbine damage accidents.

6.1. Focus on Different Knowledge Points

The results obtained from this study should be compared with the literature to showcase the contributions to knowledge. In conventional jitter control, a performance balancing method between worm gear self-locking and the yaw braking mechanism is often used to achieve limited jitter behavior [32].

To achieve a greater reduction in the jitter, similar yaw system models as those used in the present study were investigated [33–35] by using the passive flutter suppression (PFS) method, with yaw vibration and low-speed buffeting discussed. The PFS technique was executed through methods, such as the structural stiffness adjustment design, friction torque matching, and driving-torque size adjustment, etc., and analyzed by using the finite element method. Furthermore, the LSJ vibration suppression in the PFS method was only based on the assumption that the yaw motion speed was always a constant value, which was clearly only a conditional qualitative linear analysis (CQLA) approach [33].

Based on the CQLA approach, the structural parameters, first set of PD parameters, and iterative algorithm in this design were still used. Figure 10 shows the LSJ velocity fluctuations under constant yaw speeds of $\omega = 5,\ 10,\ 50$ mrad·s.

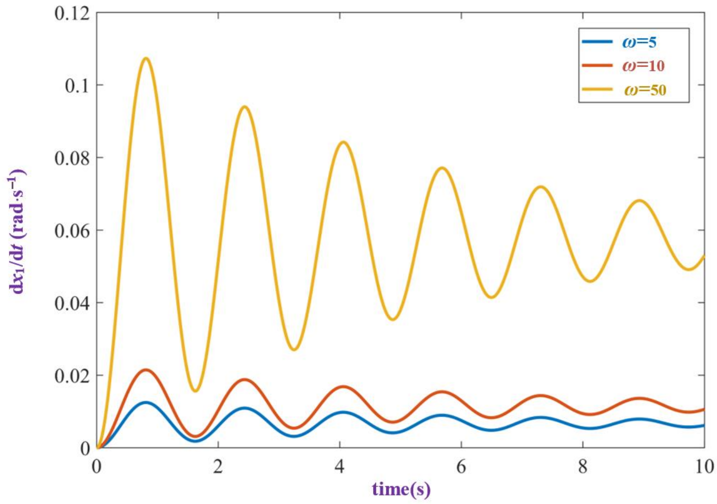

Figure 10. The LSJ velocity fluctuations under constant yaw speeds of $\omega = 5,\ 10,\ 50$ mrad·s.

It can be seen that, under different constant yaw speeds, the LSJ vibration speed can quickly converge, reflecting the effectiveness of the proposed iterative algorithm in this design. Moreover, compared with reference [33], there is no "negative" speed and no low-speed-jitter phenomenon of "back and forth" motions in the LSJ process that appear in reference [33], reflecting the robustness of the proposed iterative algorithm. It should be noted that the buffeting analysis in the present study is based on a nonlinear analysis method of "yaw-speed changing", and its superior performance is obvious compared to linear buffeting analysis methods.

As the PFS method is based on structural design and optimization, once the structure is finalized, the frequency of each order of the dynamic system is fixed. Moreover, based on the structural parameters and the first set of PD parameters in the present study, Table 3 shows the modal structure of each order of the entire dynamic system, including the control subsystem. Whether it is a tower mode or cabin mode, there is no subdivision here, but it is arranged in numerical order. The comparison is based on the PFS method, using the finite element method in reference [34,35], and the additional motor drive design, using the iterative algorithm in the present study, by directly analyzing the eigenvalues in Formula (12).

Table 3. The system model structures (method in reference [35]/algorithm in the present study).

Modal	Maximum	Standard Deviation
1	19.4700/16.5495	0.2508/0.3010
2	61.4020/52.1917	0.2387/0.2864
3	93.6540/79.6059	0.2167/0.2600
4	187.198/159.1183	0.2057/0.2468

It can be seen that, compared with the PFS system based on the finite element analysis [35], the dynamic system with active control in this study generally reduces the frequency of each order modal, which means that the vibration becomes gentle and even tends to stabilize. The damping ratios generally increase, which is a manifestation of the effectiveness of the control methods in the dynamic control systems in this study. The increase in the damping ratio is also the direct reason for the decrease in various frequencies, which offsets the elastic force and slows down the system's vibration. This is also an effective method to achieve vibration suppression from the perspective of frequency.

6.2. Focus on Different Algorithm Choices

In addition, the PID parameters have a certain physical meaning of engineering regulation; the realization of the PID control process can be realized through many ready-made commercial controller hardware devices in addition to the aforementioned PLC. This article can also provide a linear solution method for nonlinear systems. Since we were not concerned about how the third variable, $x = \theta t$, changed over time, we only treated it as an independent variable. Therefore, Equation (12) can be regarded as a linear system, which can be solved by using certain multivariable linearization algorithms. The LMI control mentioned earlier can achieve the multivariable controlled tasks in this study, in theory, and even achieve better control effects, in theory. However, due to the large number of parameters within the control algorithms, and the fact that these parameters often have no engineering physical significance, it is difficult to realize them in physical control hardware, and it is difficult to realize the on-site connection and configuration with practical engineering objects.

The LMI control has strong robustness and can realize control algorithm designs under control input constraints [36,37]. To deal with the governing system in Equation (12), the LMI algorithm is briefly analyzed as follows:

The control input signal is presented as $u = KY$, with the auxiliary Lyapunov function presented as $V = Y^{\mathrm{T}}QY$. By the proper design of Q, the convergence effect of Y can be effectively adjusted. To achieve an exponential convergence, we assume that $\dot{V} \leq -\alpha V$. Due to $V(0) = Y_0^T Q Y_0$; if $\overline{\omega} > 0$ exists, the inequality holds $Y_0^T P Y_0 \leq \overline{\omega}$, then $V(0) \leq \overline{\omega}$ is guaranteed; hence, $V(t) \leq \overline{\omega}$ can be guaranteed. The four LMIs for the calculation can be obtained as follows [36]:

$$\begin{bmatrix} \overline{\omega} & Y_0^T \\ Y_0 & N \end{bmatrix} \geq 0,\ \begin{bmatrix} k_0 N & F^{\mathrm{T}} \\ F & 1 \end{bmatrix} \geq 0,\ 0 < Q = Q^{\mathrm{T}}, \alpha N + AN + BF + NA^{\mathrm{T}} + F^{\mathrm{T}}B^{\mathrm{T}} < 0 \quad (27)$$

where $N = Q^{-1}$, $F = KQ^{-1}$, $k_0 = u_{\max}^2/\overline{\omega}$; herein, the theoretical process parameters are α, $u_{\max}$, and $\overline{\omega}$.

In the present study, to limit the change rate of control input u, we assumed that $k_1 = \dot{u}_{\max}^2/u_{\max}^2$; then, the fifth LMI could be designed as [37]:

$$\begin{bmatrix} k_1 N & (AN + BF)^{\mathrm{T}} \\ AN + BF & N \end{bmatrix} \geq 0 \quad (28)$$

solving the five LMIs in Equations (27) and (28) based on the selected theoretical process parameters, α, $u_{\max}$, and $\overline{\omega}$, the convergent state variable Y could be obtained.

Figure 11 illustrates the results of the controlled displacements by solving the LMIs; the control input signals (u_1 and u_2) and the changes in the control input signals can be obtained with the selected process parameters of $\alpha = 200$, $u_{\max} = 0.001$, and $\overline{\omega} = 0.001$. In terms of appearance, LMI control achieved a better result than the previous iterative algorithm control result. However, it should be noted that this is an ideal result after many manual selection and testing performances of the process parameters. In fact, such manual and artificial selections of three process parameters had no practical engineering significance. In terms of the implementation of the algorithm itself, it was also difficult to be successfully implemented in the PLC, which also increased the difficulty of engineering applications. For example, we noticed $u_{\max} = 0.001$ Nm, which in fact made it impossible to start the yaw movement, and that the value of α was too large, so the PLC had no way of selecting the corresponding external communication planning and related external actuators to match this physical process.

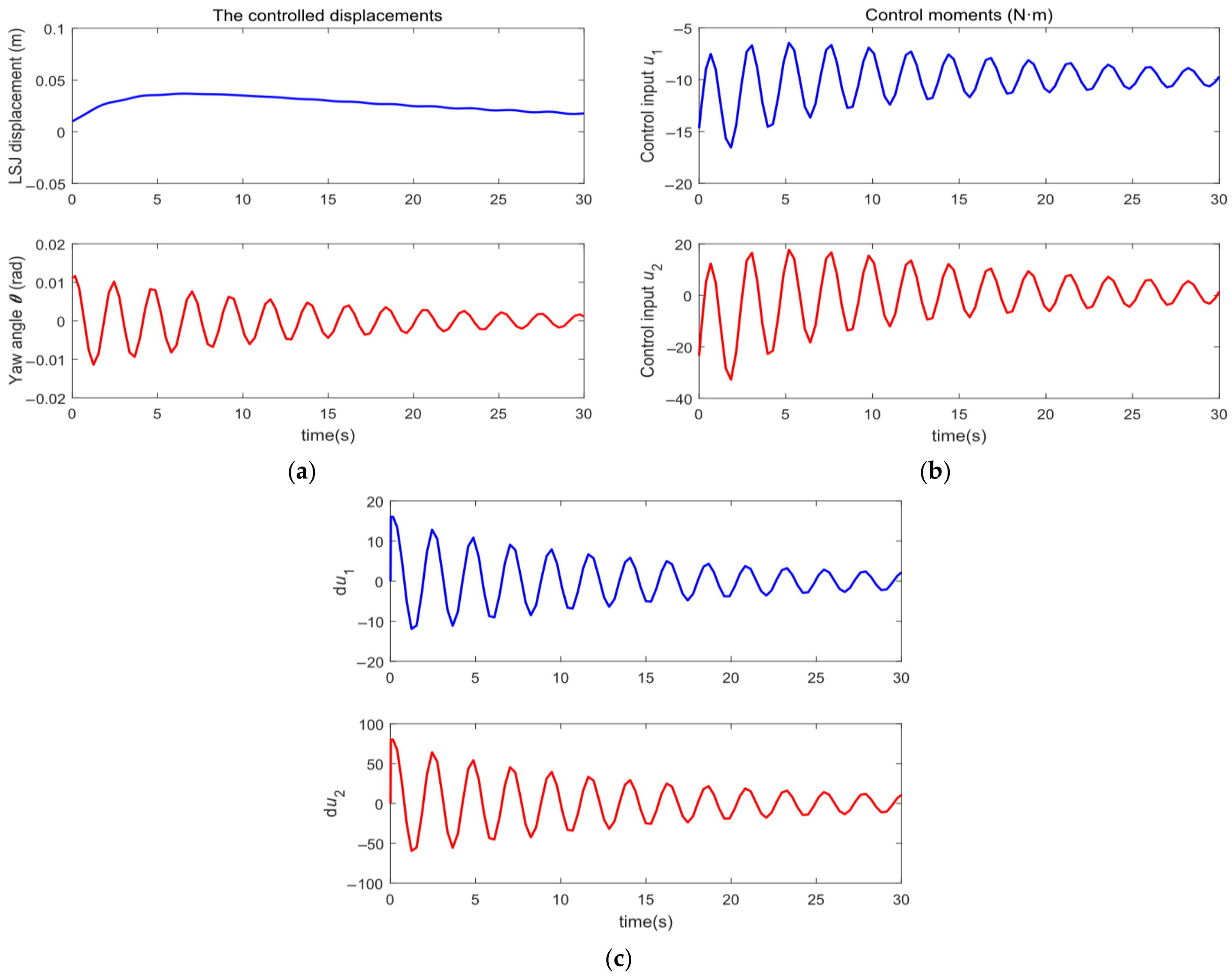

Figure 11. Illustrations: (**a**) results of the controlled displacements by solving LMIs; (**b**) control input signals (u_1 and u_2); (**c**) changes in the control input signals with the selected process parameters of $\alpha = 200$, $u_{\max} = 0.001$, and $\overline{\omega} = 0.001$.

In short, the intelligent control algorithm based on the PD adjustment had more significance concerning the physical process and advantages of the physical implementation, which was verified by the experiement mentioned earlier.

7. Further Discussion

Based on the goals of engineering applications, potential challenges or issues in HITL simulations need to be further discussed.

- Due to the limited memory of the PLC, many complex intelligent control algorithms cannot be directly run, which can lead to hardware memory overflow errors or a loss of control effectiveness due to long software scanning cycles. And, the iterative algorithm in this article is one of such complex algorithms, so we adopted a refined HITL technique [30]. The main program of the iterative algorithm will still run in the MATLAB environment, while only the algorithms related to the PD controller will be run in PLC hardware. On the one hand, this solves the problem of hardware memory overflow errors and avoids the disadvantage of long software scanning cycles. On the other hand, due to the built-in PD control unit and complex hardware interface communication functions of the PLC, it enhances the real-time adaptability of the PLC hardware. As iterative algorithms themselves are complex algorithms, other similar complex intelligent control algorithms can also apply this refined HITL technology to achieve optimized control functions. Of course, for various conventional optimization algorithms and technologies, such as optimal trajectory control technology [38], the entire intelligent control algorithm can be directly implemented in the PLC through programming, fully reflecting the real-time adaptability of PLC hardware.

- There are still many constraints or limitations that algorithms face in the process of transitioning from simulation to hardware. In addition to the constraints of the hardware memory overflow errors and long software scanning cycles mentioned above, the difficulty of programming and implementing the entire intelligent control algorithm in the PLC is also significant. There are various programming methods, and some simple algorithms can be programmed directly, according to the ladder diagram programming principles of the PLC. For some algorithms with high programming difficulties, indirect programming and the conversion to ladder diagrams can also be used to create them. For example, algorithms can be implemented under the SIMULINK architecture, and then algorithm programs based on the SIMULINK architecture can be converted into PLC controller programs to achieve online communication with the simulation environment and algorithm execution. The specific steps are as follows: first, Simulink ® PLC CoderTM tool (MathWorks, Natick, MA, USA) compiles the MATLAB code embedded in SIMULINK (embedded in S-function form) as a whole and directly compiles it into a hardware-independent IEC 61131 [39] structured text (ST). Secondly, the code generated in an ST format has the clarity and efficiency of a professional handwritten code. On this basis, make appropriate modifications and modify it to the "New ST" text suitable for the operation of the S7-300 PLC-CPU314. Finally, compile and deploy the new ST text directly on the S7-300 PLC-CPU314, which can also be converted into a ladder program before application, or modified further to be applied to the S7-200 PLC.
- The iterative algorithm can adapt to different wind conditions under dynamic changes in wind power and is fully applicable to turbine-controlled objects with repetitive motion, because it does not rely on the precise mathematical model of the system and can handle nonlinear, strongly coupled, dynamic, aeroelastic systems with high uncertainty [38]. For the current system, only an uncertain disturbance term needs to be added to Formula (11) to verify the robustness of the iterative algorithm. In addition, as mentioned earlier, common yaw mechanisms are divided into the sliding bearing type and rolling bearing type. The method proposed in this article is also applicable to rolling bearing types. In the load of rolling bearings, due to the very small dynamic friction coefficient of rolling bearings, $T\Delta\mu$ in Formula (8) can be ignored, so the corresponding auxiliary motor torque is much lower than $0.2u$. The iterative algorithm proposed in this article is still applicable and has scalability for different turbine configurations.
- The choice of PD control system instead of other types of control systems in this article does not mean that the PD controller itself has a higher precision control effect; but, because the PLC has a built-in PD module, it can be combined with high-precision intelligent control algorithms through the OPC communication, as shown in Figure 12. On the one hand, this can not only achieve high control accuracy, but can also combine control algorithms with the rich external hardware interface functions of the PLC, making it more suitable for engineering applications. In addition, the PD controller adopts open-loop control instead of closed-loop control, which does not mean that the accuracy of the open-loop control is higher, but because the open-loop control reduces the feedback link of signals, it can accelerate the algorithm execution speed, reduce the PLC scanning cycle, and better meet the real-time requirements of engineering applications. This article precisely demonstrates that the accuracy of open-loop control can fully meet the control requirements of LSJ vibrations. As for the parameters of the PD control system, we adopted the proportional derivative control based on a single neuron (PDC/SN) with an improved Hebb learning algorithm. Please refer

to reference [30] for the specific implementation process, with the steady-state error value within the range of [0 0.005].

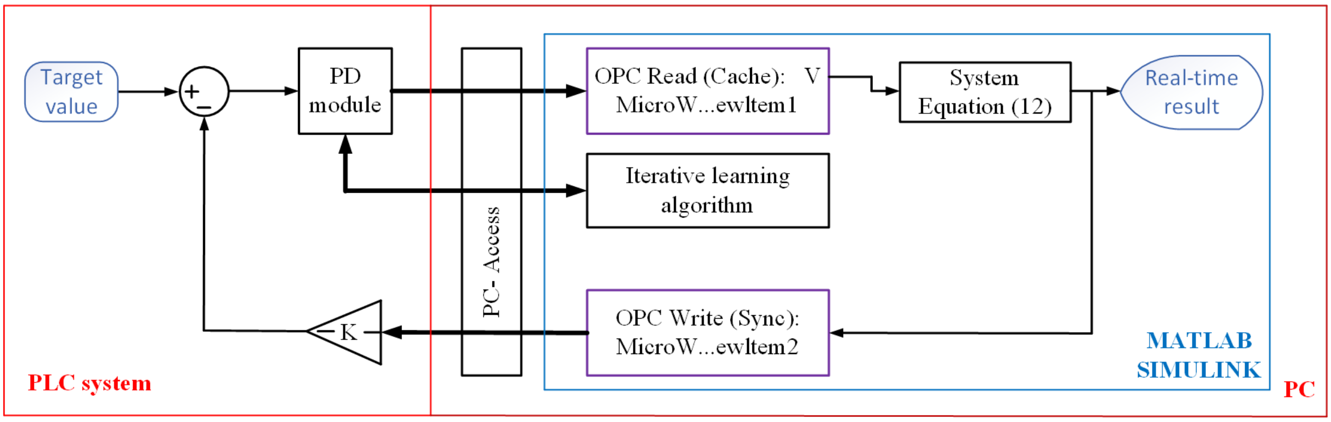

Figure 12. The implementation and validation steps of the C-HITL platform.

- To ensure consistency between the theoretical simulation and actual hardware implementation, Figure 12 shows the implementation and validation steps of the C-HITL platform. The PLC system and simulation environment can communicate with each other through the OPC server built by PC-Access. Items built in PC-Access occupy specific addresses corresponding to the PLC memory space. OPC Read/Write blocks in the simulation environment can read or write signals from or into the PLC system by connecting corresponding items built in PC-Access. The data structure and variable type defined in different connection links must be consistent with each other in the storage performance. To ensure the appropriate accuracy and moderate computing time, the sampling time must be less than 0.5 s. The communication parameters of the HITL platform considered encompass a number of features, such as (a) the synchronous OPC write mode, with a sample time of 0.1 s; (b) the OPC read mode from the cache, with a sample time of 0.1 s, with the data type being "Single"; (c) the data addresses defined in PC-Access as a type of double word, with the data type being the real type; and (d) the data variables defined in the HMI scheme being "I/O real", with data type being float, with a sample time of 0.1 s.

8. Conclusions

In this study, to suppress the nonlinear LSJ vibration that occurs on the basis of yaw crawling, a new type of additional motor-driving design is created. The nonlinear system based on the iterative learning control method of the time-varying continuous system are solved and investigated. Some concluding remarks can be drawn from the results.

- In the present study, on the one hand, an additional driving torque method is used to suppress the amplitude of the LSJ, which is a new type of additional driving design based on auxiliary motors to achieve nonlinear LSJ suppression. This design scheme is rarely mentioned in the relevant literature. On the other hand, an iterative algorithm based on an open-loop PD is used to achieve jitter suppression by using MATLAB/SIMULINK and its external communication functions;
- Detailed discussions are conducted on the accuracy, speed, effectiveness, and mathematical methods of the iterative algorithm. In order to verify the feasibility of the intelligent iterative algorithm in practical applications in this study, a C-HITL experimental platform based on OPC communication and PLC controller hardware is adopted, and the consistency between the theoretical simulation and experimental results is verified through the HMI connected to the experimental platform;
- The LSJ nonlinear system is converted into an underactuated system, and then it is processed by an iterative algorithm based on open-loop PD to meet the comprehensive requirements of precision, speed, and reliability. In the C-HITL platform based on the

OPC, the iterative algorithm runs on a PC, while the PD algorithm runs on the built-in PD module of the PLC, which seems to be able to achieve more effective and faster engineering applications, providing new ideas for the engineering application of other intelligent algorithms;
- In the iterative algorithm proposed in the present study, different sampling steps based on the Solver improvement and large-step hardware sampling are used to describe engineering applications, and compared with theoretical simulation results, obtaining reliable and consistent results.
- Once again, it is emphasized that LSJ vibration control is a rarely studied topic, but its harmfulness is becoming increasingly apparent under extreme working conditions. At present, some studies on LSJ control are based on a qualitative control method established on the basis of constant-speed yaw angle control. The LSJ control in this study is a comprehensive control method based on the nonlinear LSJ displacement and nonlinear yaw angle, accompanied by a dynamic lubrication scheme synchronously driven by the auxiliary motor. With the use of a fast-iterative learning algorithm based on solver acceleration, it has more important engineering practical significance and is easy to handle in extreme working conditions.

Author Contributions: T.L. conceived the original idea and wrote the manuscript; Z.N. and T.L. jointly supervised the study. All authors have read and agreed to the published version of the manuscript.

Funding: This research was funded by the Natural Science Foundation of Shandong Province of China, grant number ZR2022ME093.

Institutional Review Board Statement: Not applicable.

Informed Consent Statement: Not applicable.

Data Availability Statement: The data presented in this study are available in article.

Conflicts of Interest: The authors declare that there is no conflicts of interests.

References

1. Weather Network TV Station, Latest News of Typhoon Dandelion No. 16 in 2021. Available online: http://www.15tqw.com/news_7571.shtml (accessed on 29 April 2023).
2. Liu, T.; Cui, Q.; Zhao, K.; Gong, A. Stall nonlinear aeroelastic effects and active control of thin-walled composite blade with piezoelectric patches embedded. *Proc. Inst. Mech. Eng. Part G J. Aerosp. Eng.* **2023**, *237*, 2054–2073. [CrossRef]
3. Bianchini, A.; Balduzzi, F.; Rosa, D.D.; Ferrara, G. On the use of Gurney Flaps for the aerodynamic performance augmentation of Darrieus wind turbines. *Energy Convers. Manag.* **2019**, *184*, 402–415. [CrossRef]
4. Hayat, K.; Alvaro, G.M.L.; Moriones, C.D.; Ha, S.K. Flutter performance of bend–twist coupled large-scale wind turbine blades. *J. Sound Vib.* **2016**, *370*, 149–162. [CrossRef]
5. Dou, B.; Guala, M.; Lei, L.; Zeng, P. Wake model for horizontal-axis wind and hydrokinetic turbines in yawed conditions. *Appl. Energy* **2019**, *242*, 1383–1395. [CrossRef]
6. Engineering Thermophysics Research Institute. Progress in Research on the Damage of Coastal Wind Turbines under Extreme Wind Conditions at the Institute of Engineering Thermophysics. Available online: http://www.china-nengyuan.com/tech/86998.html (accessed on 20 February 2024).
7. Meng, L. Study on the structure and materials of the large-scale wind turbine tower. *J. Bengbu Univ.* **2018**, *7*, 76–80.
8. Sadowski, A.J. On the advantages of hybrid beam-shell structural finite element models for the efficient analysis of metal wind turbine support towers. *Finite Elem. Anal. Des.* **2019**, *162*, 19–33. [CrossRef]
9. Zhu, J.; Zhou, Z.; Cai, X. Multi-objective aerodynamic and structural integrated optimization design of wind turbines at the system level through a coupled blade tower model. *Renew. Energy* **2010**, *150*, 523–537. [CrossRef]
10. Ajaei, B.B.; Soyoz, S. Effects of preload deficiency on fatigue demands of wind turbine tower bolts. *J. Constr. Steel. Res.* **2020**, *166*, 105933. [CrossRef]
11. Uchida, T.; Shibuya, K.; Richmond-Navarro, G.; Calderón-Muñoz, W.R. A wind tunnel investigation of yawed wind turbine wake impacts on downwind wind turbine performances and wind loads. *Wind Eng.* **2023**, *47*, 655–670. [CrossRef]
12. Shen, L.; Huang, D.; Wu, G. An investigation of lateral-directional departure behavior based on yawing–rolling coupled wind tunnel tests. *Proc. Inst. Mech. Eng. Part G J. Aerosp. Eng.* **2018**, *232*, 2989–3000. [CrossRef]
13. Le, T.Q.; Lai, Y.C.; Voutsinas, S.G.; Yeh, C.L. Adaptive tracking control based on neural approximation for the yaw motion of a small-scale unmanned helicopter. *Int. J. Adv. Robot. Syst.* **2019**, *16*, 21–32. [CrossRef]

14. Roshanbin, A.; Preumont, A. Yaw control torque generation for a hovering robotic hummingbird. *Int. J. Adv. Robot Syst.* **2019**, *16*, 1–14. [CrossRef]
15. Saunders, B.; Nagamune, R. Fatigue load minimization for a position-controlled floating offshore wind turbine. *J. Mar. Sci. Eng.* **2023**, *11*, 2274. [CrossRef]
16. Elkodama, A.; Ismaiel, A.; Abdellatif, A.; Shaaban, S.; Yoshida, S.; Rushdi, M.A. Control methods for horizontal axis wind turbines (HAWT): State-of-the-art review. *Energies* **2023**, *16*, 6394. [CrossRef]
17. Dai, J.; He, T.; Li, M.; Long, X. Performance study of multi-source driving yaw system for aiding yaw control of wind turbines. *Renew. Energy* **2021**, *163*, 154–171. [CrossRef]
18. Song, D.; Li, Z.; Wang, L.; Jin, F.; Huang, C.; Xia, E.; Rizk-Allah, R.M.; Yang, J.; Su, M.; Joo, Y.H. Energy capture efficiency enhancement of wind turbines via stochastic model predictive yaw control based on intelligent scenarios generation. *Appl. Energy* **2022**, *312*, 118773. [CrossRef]
19. Zong, H.; Agel, F.P. Experimental investigation and analytical modelling of active yaw control for wind farm power optimization. *Renew. Energy* **2021**, *170*, 1228–1244. [CrossRef]
20. Zhao, Y.; Gong, X.; Wang, J.; Zhang, L.; Bai, Y. Stress characteristics of horizontal-axis wind turbine blades under dynamic yaw. *Appl. Sci.* **2023**, *13*, 8418. [CrossRef]
21. Zhang, Y.; Wang, Z.; Wang, Y.; Zhang, C.; Zhao, B. Research on automobile four-wheel steering control system based on yaw angular velocity and centroid cornering angle. *Meas. Control* **2022**, *55*, 49–61. [CrossRef]
22. Liu, L.; Zhang, L.; Pan, G.; Zhang, S. Robust yaw control of autonomous underwater vehicle based on fractional-order PID controller. *Ocean Eng.* **2022**, *257*, 111493. [CrossRef]
23. Sun, C.; Xu, Z.; Deng, S.; Tong, B. Integration sliding mode control for vehicle yaw and rollover stability based on nonlinear observation. *Trans. Inst. Meas. Control* **2022**, *44*, 3039–3056. [CrossRef]
24. Zhao, P.; Gao, S.C.; Bu, J.L.; He, C. *Dynamics of Large Wind Turbine*; Science Press: Beijing, China, 2018; pp. 37–88.
25. Liu, J. *Robot Control System Design and MATLAB Simulation. The Basic Design Method*; Tsinghua University Publishing Company: Beijing, China, 2017; pp. 134–166.
26. Zaitceva, I.; Andrievsky, B. Methods of intelligent control in mechatronics and robotic engineering: A survey. *Electron* **2022**, *11*, 2443. [CrossRef]
27. Feng, L.; Chai, Y.; Xu, S.; Zhang, K.; Yang, J.M. Iterative learning based intermittent fault estimation for a class of linear uncertain repeated systems. *Acta Autom. Sin.* **2020**, *46*, 307–319.
28. PENGky. Wind Turbine Yaw System. Available online: https://www.pengky.cn/fengdian-SPZ/21-yaw-system/yaw-system.html (accessed on 17 January 2024).
29. Yuanzhan Finance. Simultaneous Application of Lubrication and Hydraulic, a Centralized Lubrication System. Available online: https://baijiahao.baidu.com/s?id=1780361385531052157&wfr=spider&for=pc (accessed on 16 January 2024).
30. Liu, T. Vibration control and trajectory tracking for nonlinear aeroelastic system based on adaptive iterative learning control. *Noise Vib. Worldw.* **2022**, *53*, 390–403. [CrossRef]
31. MathWorks. Integration Method-Integration for Nonadaptive odeN Variable-Step Solver. Available online: https://ww2.mathworks.cn/help/simulink/gui/integrationmethod.html?searchHighlight=odeN&s_tid=srchtitle_support_results_1_odeN (accessed on 16 January 2024).
32. Chen, L. Functionality Investigation and Expansion of 5kW Wind Turbine Yaw and Vibration Sensors. Bachelor's Thesis, Murdoch University, Perth, Australia, 2017; pp. 10–20.
33. Li, X.; Zhao, P. Characteristics of low jitter kinematic for megawatt wind power yaw system. *J. Cent. South Univ.* **2013**, *44*, 89–94.
34. Zhang, J. Analysis on Vibration Characteristics of Yaw System and Tower of Wind Turbine. Ph.D. Thesis, North China Electric Power University, Beijing, China, 2018; pp. 22–35.
35. Zhang, B.; Jia, Z.; Yu, Z.; Zhao, B. Dynamic analysis of yaw system for small wind turbines. *Acta Energiae Solaris Sin.* **2021**, *42*, 387–393.
36. Liu, T.; Gong, A. Vibration control of cantilever blade based on trailing-edge flap by restricted control input. *Meas. Control* **2021**, *54*, 231–242. [CrossRef]
37. Liu, J.; Liu, Z. *Control System Design, Analysis and MATLAB Simulation Based on LMI*; Tsinghua University Publishing Company: Beijing, China, 2022; pp. 66–82.
38. Liu, J. *Robot Control System Design and MATLAB Simulation. The Advanced Design Method*, 2nd ed.; Tsinghua University Publishing Company: Beijing, China, 2023; pp. 97–113, 139–185.
39. Liu, T.; Sun, C.; Li, S.; Zhang, X.; Liu, G. Active control method of trailing-edge flap for suppressing high-frequency vibration of wind turbine blades. *Adv. Eng. Sci.* **2021**, *53*, 166–174.